APPROACH TO THE IRON-CATALYZED FORMATION PROCESS OF N_2 FROM HETEROCYCLIC NITROGEN IN CARBON BY USE OF XRD AND XPS METHODS

Yasuhiro Ohshima, Ye Wang, Naoto Tsubouchi, and Yasuo Ohtsuka
Research Center for Organic Resources and Materials Chemistry
Institute for Chemical Reaction Science, Tohoku University
Katahira, Aoba-ku, Sendai 980-8577, JAPAN

KEYWORDS: Fuel nitrogen, iron catalyst, X-ray diffraction analysis

ABSTRACTS

PAN-derived carbon as a model of coal char has been heated in high purity He, and the catalysis of N_2 formation by precipitated iron has been investigated by means of TEM, XPS and XRD. Nanoscale iron particles are very active for this reaction at 600 – 1000℃. The XPS and XRD analyses after heat treatment reveal that nitrogen functionality does not change significantly but carbon crystallization takes place via the dissolution of iron into the carbon substrate. The *in situ* XRD measurements during heating show the formation of solid solution of iron and nitrogen (and carbon). The iron-catalyzed conversion of heterocyclic nitrogen to N_2 probably proceeds through formation of the solid solution and subsequent decomposition into N_2.

INTRODUCTION

The nitrogen present in coal (coal-N) is emitted as NO_x and N_2O during combustion. The NO_x has been implicated in acid rain and photochemical smog. In conventional pulverized coal-fired plants, 75 – 95 % of the NO_x emitted originates from coal-N. The N_2O is known to be involved in the green house effect and the ozone layer depletion. The concentration of N_2O is much higher in fluidized bed combustion that can be operated at lower temperatures (< 1000°C) than in pulverized coal-fired boilers. The N_2O arises from coal-N alone. When coal is fed into a combustion chamber, the devolatilization (pyrolysis) first takes place. In this process, part of coal-N is released as tar-N, and the remainder is retained as char-N, some of the tar-N being subsequently decomposed into HCN and NH_3 [1,2]. All these nitrogen species are the precursors of NO_x and N_2O. If coal-N can be converted efficiently to N_2 upon devolatilization, the emissions of NO_x and N_2O can greatly be reduced during subsequent combustion.

The present authors' group has found that FeOOH precipitated on low rank coals can drastically catalyze conversion of coal-N to N_2 in the fluidized bed pyrolysis at $\geqq$750°C [3,4]. We have also shown that Fe-containing minerals in low rank coals, probably as ion-exchanged forms, can also promote N_2 formation in the fixed bed pyrolysis at almost the same temperature range as above [5,6]. Since N_2 formation occurs dominantly after complete release of volatile-N (tar-N, HCN, and NH_3), it is strongly suggested that the iron derived from Fe-containing minerals as well as FeOOH catalyzes conversion of char-N to N_2. However, the detailed mechanism is not clear. The present work therefore focuses on making clear the Fe-catalyzed formation process of N_2 at solid phase by using PAN-derived carbon as a model of coal char.

EXPERIMENTAL

Pure carbon without any minerals was used in place of coal char in order to avoid their influences on N_2 formation. The carbon was prepared by carbonization of PAN for 30 min at 1000°C, followed by activation in 20 vol% O_2 at 500°C. The C, H and N contents in the carbon with size fraction of 44 – 74 μm were 79.3, 0.4 and 6.8 wt%, respectively, the BET surface area determined by N_2 adsorption being 480 m^2/g. Fine particles of FeOOH were precipitated onto the carbon from an aqueous solution of $FeCl_3$ by using $Ca(OH)_2$ [7].

The carbon (180 mg) with or without 1.9 wt% Fe was heated with a fixed-bed quartz reactor in a

stream of high purity He (> 99.9999 %) at 10°C /min up to 1000°C, and N_2 evolved was determined on line at 5 min intervals with a high speed micro GC. Detailed procedures have been described elsewhere [5]. The samples before and after heat treatment were characterized by TEM, XPS and XRD. The *in situ* XRD measurements were also made with Mn-filtered Fe-K α radiation during heating the Fe-loaded carbon under the same conditions as above.

RESULTS AND DISCUSSION

Formation of N_2. Figure 1 shows the temperature-programmed profiles for N_2 formation. The iron remarkably promoted conversion to N_2 at 600 – 1000°C. The catalytic effect appeared at a lower temperature of around 600°C than observed with low rank coals [3,4], probably because of a lower heating rate in the present work. The rate of N_2 formation reached the maximal value at 800°C and then decreased. The rate at 800°C with 1.9 wt% Fe was about 10 times that without catalyst. The presence of the iron almost doubled N_2 yield after 60 min soaking at 1000°C, the yield being 32 and 63 % without and with 1.9 wt% Fe, respectively.

XPS spectra. The N 1s XPS spectra were measured to examine the change in nitrogen functionality upon heat treatment, and least-squares curve fitting of the spectra was performed using Gaussian peak shapes [8]. Pyrrolic-N (398.7$\pm$0.1 eV) and pyridinic-N (400.3$\pm$0.1 eV) were the main nitrogen forms in the original carbon before heat treatment. The ratio was almost unity, which was much lower than that observed for brown coal char after pyrolysis at 900°C [8]. When the carbon with 1.9 wt% Fe was heated at 600 – 1000°C, the distribution of pyrrolic-N, pyridinic-N and quaternary-N (401.4$\pm$0.1 eV) was significantly unchanged. This suggests that N_2 evolves from these species at almost the same rate. On the other hand, the iron precipitated on brown coal is effective for preferential formation of N_2 from pyrrolic-N [8]. The difference may be related with a larger ratio of pyrrolic-N/pyridinic-N in the latter case.

TEM observations. The average size of iron particles at 600°C, that is, before the start of N_2 formation, was as fine as 15 nm. When the iron was precipitated onto PAN-derived carbon without O_2-activation in the same manner as above, the average particle size was much larger (70 nm), and the iron was less active. The activation increased not only the surface area but also the amount of oxygen functional groups, which lead to the formation of the more highly dispersed iron on the activated carbon. The average size increased from the initial 15 nm to 23 nm after heat treatment at 1000°C. In the size distribution, most of iron particles were initially $\leqq$20 nm in size, whereas more than half of them were $\geqq$20 nm at 1000°C, and the iron with the size of 40 – 60 nm was also observed. These observations show that iron particles move within the carbon matrix, catalyze N_2 formation, and agglomerate in this process.

XRD measurements. Figure 2 shows the XRD profiles for Fe-bearing samples cooled to room temperature after heat treatment. At 600°C, the small peaks of magnetite (Fe_3O_4) and wustite ($Fe_{1-x}O$) were observed, which means the transformation of the initial form of FeOOH to these oxide forms. At 1000°C, the oxide species disappeared, and instead the XRD lines of metallic iron (α-Fe) and cementite (Fe_3C) appeared. Not only the reduction to metallic iron but also the reaction of the iron with the carbon substrate took place between 600 and 1000°C. Figure 2 also provides information about carbon structures due to C(002) lines, which can be separated into amorphous and turbostratic carbon, denoted as A- and T-carbon respectively, by deconvolution. As the temperature increased, the proportion of T-carbon increased from 14 to 18 %. On the other hand, no significant change in C(002) lines was observed in the absence of the iron. The formation of cementite and T-carbon indicates that the iron first dissolves in the carbon substrate and subsequently catalyzes crystallization reactions [9]. It can readily be expected that the iron reacts with heterocyclic nitrogen forms in the carbon matrix.

Figure 3 shows the *in situ* XRD profiles during heating the carbon with 1.9 wt% Fe. At 655°C, metallic iron (α-Fe) was the dominant species, though the small peaks of wustite were also observed. Interestingly, the XRD lines of austenite, solid solution of γ-Fe and nitrogen

(and/or carbon), existed as well. When the temperature was raised to 815 and 1025°C, the XRD intensities of this species increased with a corresponding decrease in the intensity of metallic iron, and austenite was the predominant form in this temperature region. When the sample heated at 1025°C was quenched to room temperature, metallic iron and cementite were formed, in harmony with the XRD profile given in Figure 2.

Mechanism. It should be noted that the catalysis of conversion to N_2 by iron (Figure 1) and the formation of austenite (Figure 3) occur at almost the same temperature range. According to phase diagrams of Fe-N and Fe-C [10], nitrogen can dissolve rapidly into iron at a lower temperature of about 590°C, compared with that (740°C) for carbon. The former temperature corresponded well to the onset of the Fe-catalyzed formation of N_2. It is thus likely that the austenite observed at < 740°C is the solid solution of Fe and N, and that N_2 formation in this temperature range proceeds through the intermediate. The austenite may be transformed to iron nitrides (Fe_xN), which can readily be decomposed into N_2 because of thermal instability [8]. The austenite formed at $\geqq$740°C may be composed of Fe, N and C, and converted to Fe_xN_yC as well as Fe_xN. The decomposition of Fe_xN_yC into N_2 may involve carbon crystallization, that is, the formation of turbostratic carbon (Figure 2). The presence of such crystallized carbon might prevent iron particles from moving within the carbon matrix. As mentioned above, the TEM observations revealed that catalyst agglomeration took place in the process of N_2 formation. The lowering in both mobility and activity of iron particles may be responsible for the decreased rate of N_2 formation observed after 800°C (Figure 1).

CONCLUSIONS

Fine iron particles with the average size of 15 nm promote remarkably N_2 formation from PAN-derived carbon during heating in an inert gas at 600 – 1000°C. Catalyst agglomeration occurs in this process. The XPS spectra show that pyrrolic-N and pyridinic-N are the main forms, and that such nitrogen functionality is significantly unchanged upon heat treatment. The XRD analyses reveal the transformation of amorphous to turbostratic carbon, meaning the dissolution of the iron into the carbon substrate. Furthermore, the *in situ* XRD measurements during heating show the formation of austenite that is solid solution of iron and nitrogen (and carbon). It is likely that iron nanoparticles move in the carbon matrix and react with heterocyclic nitrogen to form the solid solution, which is subsequently decomposed into N_2.

ACKNOWLEDGMENTS

The present work was supported in part by the Proposal-Based New Industry Creative Type Technical R&D Promotion Program from the New Energy and Industrial Technology Development Organization (NEDO), Japan. The authors acknowledge the assistance of Ms. Hazuki Satake in carrying out experiments.

REFERENCES

1 Davidson, R.M. In *Nitrogen in Coal*; IEAPER/08; IEA Coal Research: London, 1994.
2 Leppälahti, J.; Koljonen, T. *Fuel Processing Technology* **1995**, *43*, 1.
3 Ohtsuka, Y.; Mori, H.; Watanabe, T.; Asami, K. *Fuel* **1994**, *73*, 1093.
4 Mori, H.; Asami, K.; Ohtsuka, Y. *Energy Fuels* **1996**, *10*, 1022.
5 Wu, Z.; Ohtsuka, Y. *Energy Fuels* **1997**, *11*, 477.
6 Wu, Z.; Ohtsuka, Y. *Energy Fuels* **1997**, *11*, 902.
7 Ohtsuka, Y.; Asami, K. *Catalysis Today* **1997**, *39*, 111.
8 Ohtsuka, Y.; Watanabe, T.; Asami, K.; Mori, H. *Energy Fuels* **1998**, *12*, 1356.
9 Oya, A.; Marsh, H. *J. Mater. Sci.* **1982**, *17*, 309.
10 Massalski, T.B. In *Binary Alloy Phase Diagrams*; Vol. 2; ASM International: Ohio, 1990.

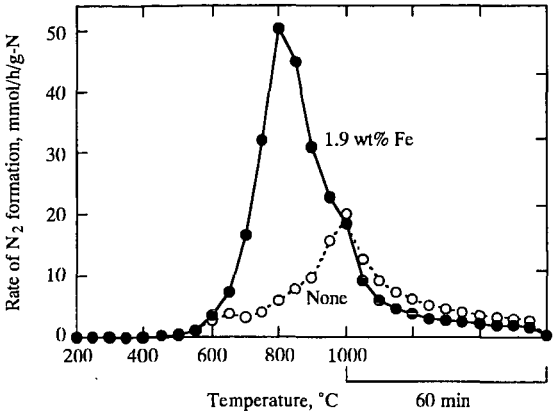

Figure 1 N_2 formation during temperature programmed heat treatment of PAN-derived carbon.

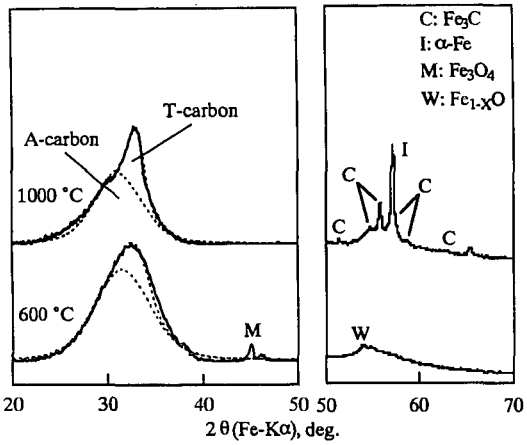

Figure 2 XRD results for Fe-bearing samples cooled to room temperature after heat treatment.

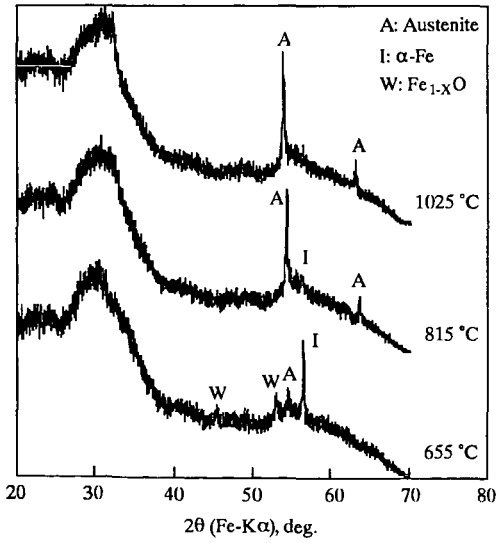

Figure 3 *In situ* XRD profiles during heating of Fe-bearing carbons.

Characterization of Peats by X-ray and NMR Methods

S. R. Kelemen, M. Afeworki and M. L. Gorbaty
Exxon Research and Engineering Company
Annandale, NJ 08801

A. D. Cohen
U. of South Carolina
Dept. of Geological and Environmental Sciences
Columbia, SC 29208

Keywords: Peat, XPS, Solid State ^{13}C NMR

X-ray photoelectron spectroscopy (XPS), X-ray absorption near edge structure (XANES) spectroscopy and solid state CP MAS ^{13}C NMR spectroscopy have proven to be viable non-destructive techniques for quantifying heteroatom functionalities in complex carbonaceous systems. Coals and kerogens have been examined extensively by these techniques. However, much less attention has been given to diagenetic stage precursors of these fossil materials. In this work, a set of eight well-defined peat samples has been examined by X-ray and NMR methods. Oxygen is by far the most abundant heteroatom species in peat derived from lignin and cellulose materials. A combination of XPS and NMR methods has been examined for quantifying organic oxygen species in peat. Total organic oxygen determined by XPS was significantly less than the amount obtained from oxygen determined by difference. XPS and NMR results confirm that carbon bonded to a single oxygen species are the predominant form in all peat samples studied and that multiply bonded carbon oxygen species make up only 25% of the oxygen population in these peat samples. The advantages of a multiple technique approach for quantifying organic oxygen forms in carbonaceous solids is discussed.

I. Introduction

X-ray and NMR are viable non-destructive techniques for quantification of organic nitrogen, sulfur and oxygen species in complex carbonaceous systems. For coal and kerogen, chemistry of heteroatom transformations is important for understanding both geological and utilization processes. Next to carbon and hydrogen, oxygen is usually the most abundant atom in organic sedimentary material. Nevertheless, determining the amount and kinds of organic oxygen species remains a formidable analytical challenge for these materials. Total organic oxygen is usually determined by difference [1]. Other methods involve fast neutron activation analysis for oxygen corrected for inorganic forms or pyrolysis followed by coulometry [1]. Infrared spectroscopy [2-4], solid-state (SS) ^{13}C NMR analysis [5] and X-ray Photoelectron Spectroscopy (XPS) [6-8] have been used to directly gain information about the kinds of organic oxygen species in coal.

Peat is a sedimentary deposit composed primarily of plant derived material and is a precursor of coal. The organic oxygen content exceeds that of coal. The physical and chemical make-up of peat varies widely and differences in organic oxygen functional group distributions are expected [9]. The present work uses a combination of XPS and SS ^{13}C NMR to quantify oxygen species in a set of eight well-defined peat samples.

II. Experimental

A) Samples

The peat samples were obtained from the peat sample bank of the University of South Carolina [9]. The elemental data for the peat samples are shown in Table 1. These peats differ significantly in composition due to the variety of source plants and depositional settings. The fresh starting coal samples were obtained in sealed ampoules from the Argonne Premium Coal Sample Program [10]. Other coal samples were obtained from the Penn State coal sample bank [11]. The elemental data for these coals are included in Table 1.

B) X-ray Photoelectron Spectroscopy

The XPS spectra were obtained with a Vacuum Generators (VG) ESCA Lab system using Al K alpha non-monochromatic radiation and a five channel detection arrangement. The samples were evacuated to remove moisture and ground into fine powders. The powders were mounted on a metallic nub via non-conducting double-sided tape. An energy correction was made to account for sample charging based on the carbon (1s) peak at 284.8 eV. The elemental concentrations are reported relative to carbon on an atomic basis, calculated from XPS spectra based on the area of the characteristic

photoelectron peaks after correcting for atomic sensitivity. The amount of organic oxygen was derived from the total oxygen (1s) signal by taking into account inorganic contributions [8]. The main inorganic elements observed via XPS are found in Table 2. For coal, the amount of each inorganic element determined by XPS may differ from the bulk inorganic elemental composition due to particle size effects and organic encapsulation [8].

The nature of the organic oxygen species present in lignite and lignin were determined by analyzing oxygen's effect on the XPS carbon (1s) signal of adjacent carbon atoms [8]. The level of carboxyl and carbonyl is derived from the curve resolved carbon (1s) spectrum. The amount of oxygen associated with carbon-oxygen single bond species is determined by subtracting the carboxyl and carbonyl oxygen levels from the total amount of organic oxygen. The relative amount of aromatic carbon was determined by the method of Π to Π^* signal intensity [12]. A complete list of XPS data for samples contained in this report is found in Table 2.

Five peaks were used to curve resolve the XPS carbon (1s) signal for peat. These occur at 284.8, 285.3. 286.3, 287.5, and 289.0 (±0.1) eV. The 284.8 eV peak represents contributions from both aromatic and aliphatic carbon. The 286.3 eV peak (Type I) represents carbon bound to one oxygen by a single bond (e.g., C-O, C-OH etc.). The 287.5 eV peak (Type II) corresponds to carbon bound to oxygen by two oxygen bonds (C=O, O-C-O). The 289.0 eV peak (Type III) corresponds mainly to carbon bound to oxygen by three bonds (O=C-O). The 285.3 peak will have contributions mainly from carbon adjacent to carboxyl carbon (beta peak) and carbon bound to nitrogen (i.e. pyrrole, pyridinic). The 285.3 eV peak is therefore fixed to the sum of the intensity of the 289.0 eV peak and the intensity of carbon adjacent to nitrogen (i.e. twice the nitrogen level). The results shown in Table 3 assume 1) that two oxygens are associated with the Type III carbon (1s) signal and 2) that one oxygen is associated with the Type II carbon (1s) signal. The amount of oxygen associated with the Type I carbon (1s) signal is obtained by subtracting the oxygen associated with the Type II and the III carbon (1s) signal from the amount of total organic oxygen.

C) Solid State ^{13}C NMR Spectroscopy

High-resolution solid-state ^{13}C NMR measurements of peat samples were performed using a Chemagnetics CMX-200 spectrometer operating at a static magnetic field of 4.7 T (50.2 MHz ^{13}C). Peat samples were packed into a 5-mm diameter zirconia rotor and spun at 8-kHz using dry nitrogen gas. Cross-polarization magic-angle spinning (CPMAS) NMR was used to characterize the peat samples. The CPMAS experiments were performed at a ^{1}H-^{13}C CP contact time of 3 ms and a pulse repetition delay of 2 seconds. The ^{1}H and ^{13}C radio-frequency fields for cross-polarization and the proton high power decoupling during data acquisition were at 62.5 kHz. The definition of ^{13}C NMR structural parameters and chemical shift ranges are shown in Table 4. A complete list of structural parameters obtained by solid-state ^{13}C NMR for samples contained in this report is found in Table 5.

III. Results and Discussion

The atomic H/C and O/C ratios are plotted for peat, lignite and coal in Figure 1 (called a Van Krevelan Diagram [13]). The O/C values were obtained from XPS data. All peat samples have higher H/C and O/C values than coal and lignite. These results are in good general agreement with established ordering for these materials [13]. The range of organic oxygen determined by XPS for peat is roughly between 20 and 30 oxygen per 100 carbons, (Table 3). These results are significantly lower than the amount of oxygen determined by difference, (Table 1).

A combination of XPS and SS ^{13}C NMR was used to characterize the peat samples. Figure 2 shows excellent agreement between the percent aromatic carbon determined by XPS and NMR methods. Previously published results for coal and lignite are included for comparison [12]. Not surprisingly, peat has significantly lower levels of aromatic carbon. The close correspondence between the XPS and NMR values for peat indicate that the aromatic carbon level at the surface of finely ground peat is comparable to the bulk.

XPS was used to distinguish the kinds of organic oxygen species present in peat. Table 3 shows the results based on the methodology described in the experimental section. Carboxyl oxygen accounts for roughly 1/3 of the oxygen present in peat. Carbon oxygen single bond species account for roughly half of the oxygen species. For coal, carbonyl is the predominant Type II oxygen form. This situation may be different for peat. Species such as O-C-O (present in cellulose) would contribute to the Type II carbon (1s) signal. The presence of a significant amount of O-C-O species in peat would complicate the interpretation for the amount of oxygen associated with Type II carbon (1s) signal. The C=O values listed in Table 3 therefore represent upper limits.

Table 4 provides the definition of ^{13}C NMR structural parameters based on the carbon species and chemical shift ranges. Table 5 shows results obtained for the different structural parameters as a fraction of the total ^{13}C signal. SS ^{13}C NMR parameters fa^C, (carboxyl, carbonyl, amide), fa^P (phenolic, phenoxy) and fal^O (alcohol, ether) have oxygen associated with them. The range for the percentage of carbon associated with oxygen ($fa^C + fa^P + fal^O$) in peat is 32 to 49. It is not possible to determine the total amount of oxygen relative to carbon from the sum of oxygen related ^{13}C NMR signals (fa^C, fa^P, fal^O) because it is uncertain what oxygen stoichiometry to assign to each oxygen related ^{13}C NMR signal. Nevertheless, a conservative estimate of the amount of oxygen associated with fa^C is 1.0 (i.e. carbonyl, amide etc.) and 0.5 for fa^P and fal^O (i.e., aliphatic ether, methoxy etc.). Undoubtedly other species will have a combined impact on fa^C, fa^P and fal^O. A comparison of the XPS derived total organic oxygen signal and the NMR estimate based on $fa^C + 0.5(fa^P + fal^O)$ is shown in Figure 3. The NMR parameter fa^C is expected to be related to the amount of oxygen with O-C=O (Type III) determined by XPS. Figure 3 shows a close correspondence for these XPS and NMR parameters with all peat samples. Figure 3 also shows that the amount of oxygen found with Type I plus Type II XPS species is closely related to $0.5(fa^P + fal^O)$. We would expect this correspondence if most of the oxygen species associated with the XPS Type II carbon (1s) signal are O-C-O species and if ether species predominate in fa^P and fal^O.

IV. Summary

A self-consistent interpretation of oxygen derived XPS and ^{13}C NMR signals provides insight into the kinds of oxygen species present in peat. Multiply bonded carbon oxygen species make up only 25% of the oxygen population in these peat samples. XPS and NMR results indicate that carbon oxygen single bonded species are the predominant form in all peat samples studied. It is likely O-C-O species and, in general, ether species makeup a large part of the carbon oxygen single bond population.

V. References

1) Ehmann, W. D.; Koppenaal, D. W.; Hamrin, C. E.; Jones, W. C.; Prasand, M. N.; Tian, W. Z., *Fuel* **1986**, *65*, 1563.
2) Kuehn, D. W.; Snyder, R. W.; Davis, A.; Painter, P. C., *Fuel*, **1982**, *61*, 682.
3) Reisser, B.; Starsinic, M.; Squires, E.; Davis, A.; Painter, P. C., *Fuel*, **1984**, *63*, 1253.
4) Dyrkacz, G. R.; Bloomquist, C. A.; Solomon, P. R., *Fuel*, **1984**, *63*, 536.
5) Solum, M. S.; Pugmire, R. J.; Grant, D. M., *Energy and Fuels*, **1989**, *3*, 187.
6) Clark, D. T.; Wilson, R., *Fuel*, **1983**, *62*, 1034.
7) Grint, A.; Perry, D. L., *Fuel*, **1983**, *62*, 1029.
8) Kelemen, S. R.; Kwiatek, P. J., *Energy and Fuels*, **1995**, *9*, 841.
9) Cohen, A. D.; Rollins, M. S.; Durig, J. R.; Raymond, R. JR., *J. Coal Quality*, **1991**, *10*, 145.
10) The Users Handbook for the Argonne Premium Coal Sample Program; Vorres, K. S., Ed.; Argonne National Laboratory: Argonne, IL, 1989; ANL-PCSP-89-1; *Energy and Fuels*, **1990**, *4*, 420.
11) Glick, D. C.; Davis, A., *Org. Geochem.*, **1991**, *17*, 421.
12) Kelemen, S. R.; Rose, K. D.; Kwiatek, P. *J., Appl. Surf. Sci.*, **1993**, *64*, 167.
13) Krevelen, D. W. van: Coal: Amsterdam: Elsevier, **1993**, p 181.

Table 1

Sample Peat	(per 100 C) Hydrogen	(per 100 C) Nitrogen	(per 100 C) Sulfur	(per 100 C) Oxygen*
Minn. Hem.	117	4.5	0.2	42.1
Me. Sph.	131	0.8	0.1	58.9
Lox. Nym.	130	6.3	0.5	39.1
Lox. Saw.	111	4.8	0.7	40.1
Sh. Rv. Rhiz.	118	3.9	2.8	50.4
Oke. Tax.	121	4.0	0.2	41.0
Oke. Nym.	122	5.3	0.3	39.4
N.C. 1st Col.	107	1.3	0.1	35.0
Coal/Lignite				
DECS-11 Beulah	73	1.2	0.4	31.0
DECS-25 Pust	82	1.2	0.2	17.6
PSOC-1468 Buck Mountain	16	0.8	0.2	0.9

(*) determined by difference

Table 2

Sample Peat	Aromatic Carbon	Nitrogen	Sulfur	Si	Al	Ca
Minn. Hem. (Peat) SCSB	26	2.8	0.2	0.5	0.3	--
Me. Sph. (Peat) SCSB	24	1.0	0.1	--	--	--
Lox. Nym. (Peat) SCSB	23	3.9	0.2	--	--	0.7
Lox. Saw. (Peat) SCSB	28	3.2	0.3	--	--	0.7
Sh. Rv. Rhiz. (Peat) SCSB	35	2.3	1.9	3.8	2.9	--
Oke. Tax. (Peat) SCSB	25	2.7	0.1	2.4	--	--
Oke. Nym. (Peat) SCSB	23	4.4	0.1	1.5	--	--
N.C. 1st Col. (Peat) SCSB	29	1.1	<0.1	--	--	--
Coal/Lignite						
DECS-11 Beulah	55	1.3	0.3	2.4	2.5	1.1
DECS-25 Pust	52	1.3	0.3	3.2	4.1	1.3

Table 3

Sample	Total Organic Oxygen	-O	C=O	O-C=O
Minn. Hem. (Peat) SCSB	24.2	11.3	6.7	6.2
Me. Sph. (Peat) SCSB	22.4	10.7	6.1	5.6
Lox. Nym. (Peat) SCSB	22.2	8.6	6.6	7.0
Lox. Saw. (Peat) SCSB	27.0	9.3	8.3	9.4
Sh. Rv. Rhiz. (Peat) SCSB	24.3	7.3	8.8	8.2
Oke. Tax. (Peat) SCSB	25.6	9.3	6.9	9.4
Oke. Nym. (Peat) SCSB	30.2	14.5	7.9	7.8
N.C. 1st Col. (Peat) SCSB	21.2	11.1	3.7	6.4

Table 4 - Definition of ^{13}C NMR Structural Parameters

Parameter	Chemical Shift Range (ppm)	Carbon Type
fa	90-240	Aromatic/Carboxyl/Carbonyl/Amide
fa'	90-165	Aromatic
faC	165-240	Carboxyl/Carbonyl/Amide
fa^P	150-165	Phenoxy/Phenolic
fa^S	135-150	Alkyl-Substituted Aromatic
fa^B	90-135	Bridgehead Aromatic
fal	0-90	Aliphatic
fal^H	22-50	Methylene/Methine
fal*	0-22 & 50-60	Methyl/Methoxy
fal^O	50-90	Alcohol/Ether

Table 5

	fa	fa'	faC	fa^P	fa^S	fa^B	fal	fal^H	fal*	fal^O
Minn. Hem.	0.41	0.35	0.07	0.04	0.06	0.24	0.59	0.19	0.11	0.37
Me. Sph.	0.40	0.33	0.06	0.04	0.04	0.24	0.60	0.18	0.07	0.39
Lox. Nym.	0.35	0.24	0.11	0.03	0.04	0.16	0.65	0.30	0.12	0.30
Lox. Saw.	0.43	0.33	0.10	0.05	0.06	0.22	0.57	0.20	0.11	0.33
Sh. Rv. Rhiz.	0.40	0.33	0.06	0.04	0.06	0.23	0.60	0.18	0.13	0.38
Oke. Tax.	0.38	0.29	0.09	0.04	0.05	0.19	0.62	0.30	0.10	0.28
Oke. Nym.	0.40	0.30	0.10	0.04	0.05	0.21	0.60	0.18	0.11	0.38
N.C. 1st Col.	0.45	0.36	0.09	0.05	0.07	0.23	0.56	0.33	0.09	0.18

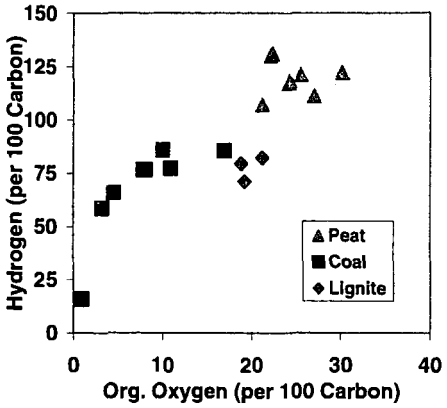

Figure 1 - H/C vs. O/C diagram for peat, and lignite. The O/C values were obtained from XPS data. H/C values are from elemental data. Previously reported results from Argonne Premium Coal are included for reference.

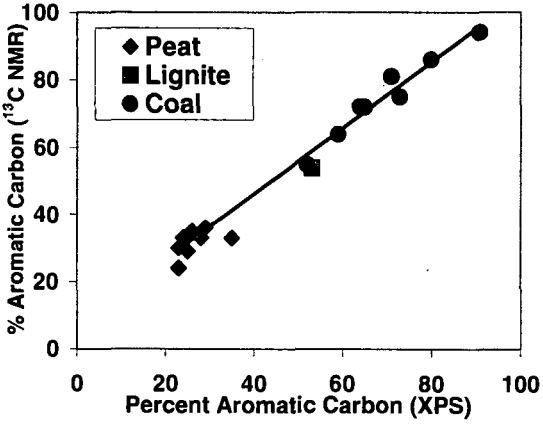

Figure 2 - Comparison of XPS and ^{13}C NMR results for aromatic carbon from peat, coal and lignite. Previously reported results for Argonne Premium Coal [12] are included for reference.

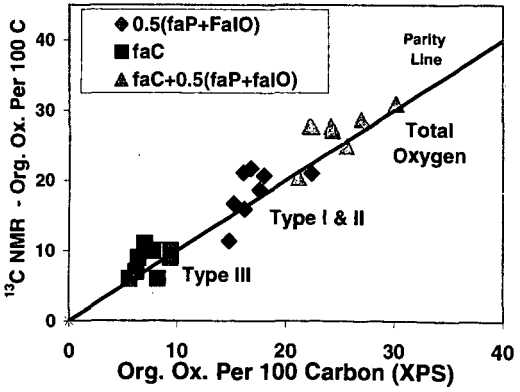

Figure 3 - Comparison of XPS and ^{13}C NMR derived parameters for organic oxygen species in peat.

SULFUR BEHAVIOR IN VARIOUS CHEMICAL TREATMENTS OF COAL

Katsuyasu Sugawara[1], Naoto Tsubouchi[1], Takuo Sugawara[1] and Masayuki Shirai[2]

1) Faculty of Engineering and Resource Science, Akita University, Akita 010-8502 JAPAN
2) Institute for Chemical Reaction Science, Tohoku University, Sendai 980-8577 JAPAN

KEYWORDS: Coal, organic sulfur, pyrolysis, pretreatment, XANES

INTRODUCTION

Coal is abundant and low-cost energy resource and deserves increasing use in developing countries. Efficient precleaning technology must be developed for the utilization of high-sulfur and low-grade coals. Sulfur is a key component not only for the environmental conservation but also for the development of new coal utilization processes. Incomplete understanding of the behavior of organic sulfur during heat treatment has given rise to a misbelief that organic sulfur in coal cannot be removed by the pretreatments.

Development of surface analyses enables us to know the actual forms of organic sulfur in coal. XANES and XPS have been demonstrated as strong tools to elucidate organic sulfur forms in coal and heavy hydrocarbons.[1-4]

We have demonstrated the dynamic behavior of sulfur forms during pyrolysis in a series of studies on chemical coal cleaning processes.[5-7] These studies showed that rapid pyrolysis removed organic sulfur effectively in some types of coal. The release rate as well as the extent of organic sulfur removal increased with the contents of exinite and vitrinite. Part of the organic sulfur exist in a thermally stable form which is difficult to remove from coal by pyrolysis. Thermally stable organic sulfur remaining in the solid should be changed to decomposable forms to achieve efficient desulfurization in the pretreatment process.

In the present study, behavior of sulfur forms has been followed for lignite, subbituminous and bituminous coals in rapid pyrolysis. Chemical pretreatments were carried out to transfer the thermally stable form of reactive species before pyrolysis. Organic sulfur forms were determined by using XANES for coal before and after rapid pyrolysis with chemical pretreatments. Sulfur capture experiment was also conducted for rapid pyrolysis char in a nitrogen stream containing hydrogen sulfide to seek a new application to porous carbon.

EXPERIMENTAL

Table 1 shows proximate, ultimate and sulfur-form analyses for the sample coals, Spanish lignite Mequinenza, Australian subbituminous Muswellbrook, Chinese bituminous Nantong, and Montana subbituminous Rosebud coals. Average particle size of the sample was 0.35 mm.

Two kinds of chemical pretreatments were carried out as follows. The coal samples were immersed in a saturated aqueous solution of potassium hydroxide for 24 h with agitation at room temperature. The wet alkali immersed samples were then heated at 523 K for 4 h in a nitrogen atmosphere after filtration from potassium hydroxide solution. The alkali-treated samples were washed repeatedly with distilled water to reduce the basicity and then dried out at 380 K.[8]

Table 1 Analyses of sample coals

Sample	Ultimate [wt%, daf]					Proximate [wt%, db]		Sulfur form [wt% of total sulfur]		
	C	H	N	S	Diff.	VM	Ash	Pyritic	Sulfate	Organic
Mequinenza	69.3	5.5	1.0	13.6	10.6	48.8	21.4	7	0	93
Muswellbrook	77.5	6.0	2.1	0.8	13.6	41.1	8.3	11	3	86
Nantong	88.9	4.9	0.6	5.0	0.6	17.0	17.3	34	1	65
Rosebud	73.0	4.5	0.9	0.9	20.7	39.8	10.2	32	3	65

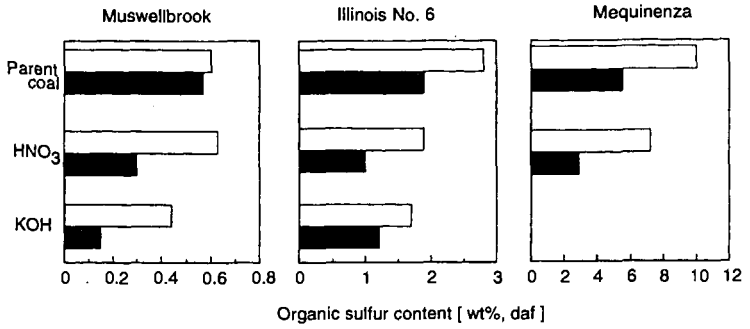

Fig.1 Change in organic sulfur content with various pretreatments
(□, before pyrolysis; ■, after pyrolysis)

Nitric acid pretreatment was also carried out. The sample coals were immersed in nitric acid aqueous solution at a boiling temperature. After filtration and drying, rapid pyrolysis was conducted for the pretreated coals by using a free-fall pyrolyzer. This apparatus enables coal particles to be heated in a nitrogen stream at rates from 10^3 to 10^4 K/s depending on particle density and diameter. The temperature was 1253 K at the isothermal section of the reactor. The details of the apparatus were described elsewhere.[6]

To investigate the effect of macerals on sulfur-form and distribution, the samples were fractionated into three density groups by sink-float in zinc chloride aqueous solution. The separated samples were repeatedly washed to remove zinc chloride, which might catalyze tar decomposition. The absence of zinc chloride in the sample was confirmed by extraction with hydrochloric acid solution.[9]

Sulfur capture behavior was investigated for rapid pyrolysis char in hydrogen sulfide/nitrogen gas mixture at 1073 K in a fixed bed.

Some improvements to ASTM(D2492) were applied to analyzing sulfur forms (pyrite, ferrous sulfide, sulfate and organic sulfur) in parent and chemically pretreated coals, and in rapidly pyrolyzed char. The details of the analytical method were reported previously .[10] Sulfur K-edge XANES was applied to specifying the forms of organic sulfur.[11] XANES measurements were carried out at beam line 2A of Photon Factory in the High Energy Accelerator Research Organization. Si(111) monochromators were used to vary the incident X-ray energy. The beam irradiated the samples fixed on a nickel plate under 10^{-3} Pa in a vacuum chamber. Data were recorded in the fluorescence mode in the region of the sulfur K-edge at room temperature. The fluorescence spectra were collected using a scintillation counter. The absolute photon energy was calibrated with the assumption that the giant resonance of K_2SO_4 appears at 2481.7 eV. The third derivatives of XANES spectra from model compounds were used as fingerprints for interpreting sulfur forms in the sample. Pyrite, ferrous sulfide, crystalline sulfur, DL-cystine, thioxane-9-one, s-methly-L-cysteine, DL-methionone sulfoxide and potassium sulfate were selected as the model compounds.

RESULTS AND DISCUSSION

Figure 1 shows change in organic sulfur content in rapid pyrolysis with the chemical pretreatments. A considerable decrease in organic sulfur was observed for rapid pyrolysis chars of nitric acid or potassium hydroxide pretreated Muswellbrook. Rapid pyrolysis of parent coal did not show appreciable change in organic sulfur. The effect of chemical pretreatments can also be found in the rapid pyrolysis of Illinois No.6 coal. The organic sulfur content decreased to one third of parent coal. While Mequinenza is well known as a lignite containing more than 10 % of organic sulfur, the rapid pyrolysis of this sample shows that about half of organic sulfur decomposes during the treatment. XANES spectra indicate large amount of disulfide in

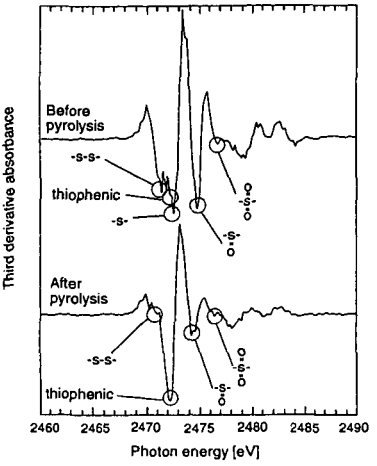

Fig.2 Sulfur K-edge XANES spectra of HNO_3 treated coal before and after pyrolysis.

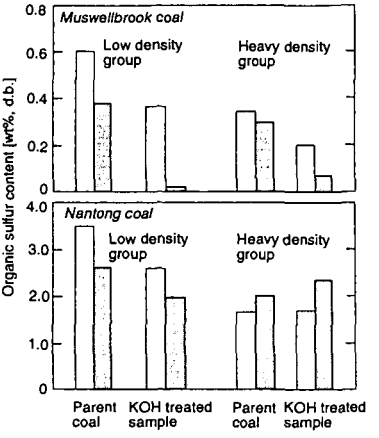

Fig.3 Effect of KOH pretretament on organic sulfur content before and after pyrolysis for density separated samples.
(□, before pyrolysis; ■, after pyrolysis)

Mequinenza coal which caused the high extent of organic sulfur removal during rapid pyrolysis. Efficient removal of organic sulfur was obtained for the combined process of rapid pyrolysis with nitric acid pretreatment. Potassium hydroxide pretreatment could not be carried out because lignite was dissolved with alkali solution.

Figure 2 shows third differential curves of XANES spectra for the nitric acid treated Illinois No.6 coal before and after rapid pyrolysis. Strong peaks are observed around 2472 eV for the coal before pyrolysis, which are attributable to disulfide, thiophene and sulfide. A strong peak at 2474.5 eV results from sulfoxide. This peak is larger than that of parent coal. After the rapid pyrolysis of nitric acid treated coal, the peaks of disulfide and sulfide disappear and the sulfoxide peak becomes small.

To investigate the effect of change in the forms and content of organic sulfur with maceral concentration on desulfurization behavior, potassium hydroxide pretreatment and rapid pyrolysis were conducted for the density separated coals of Muswellbrook and Nantong. The samples were separated into three groups (low, medium and heavy density groups): <1.26 g/cm^3; 1.26~1.40 g/cm^3; >1.40 g/cm^3 for Muswellbrook, and <1.32 g/cm^3; 1.32~1.42 g/cm^3; >1.42 g/cm^3 for Nantong coals, respectively. Figure 3 indicates change in organic sulfur content with potassium hydroxide pretreatment and rapid pyrolysis for the density separated coals. The clean char less than 0.02 % of organic sulfur was obtained for the potassium hydroxide treated sample of Muswellbrook low density group. While change in organic sulfur content was not appreciable after rapid pyrolysis of heavy density group, potassium hydroxide pretreatment was effective for change of the thermally stable organic sulfur to decomposable forms. For Nantong low density group, some extent of organic sulfur decreased with potassium hydroxide pretreatment and rapid pyrolysis. Organic sulfur content increased after rapid pyrolysis for heavy density group.

Figure 4 shows change in sulfur content of char exposed to a nitrogen stream containing hydrogen sulfide in a fixed bed at 1073 K. The sample char was obtained by rapid pyrolysis of Rosebud coal in a nitrogen stream at 1253 K. Sulfur content increased with hydrogen sulfide concentration and attained to 12 % in nitrogen gas containing 2.91 % of hydrogen sulfide. XANES analysis indicates that adsorbed sulfur formed organic sulfur in the solid phase.

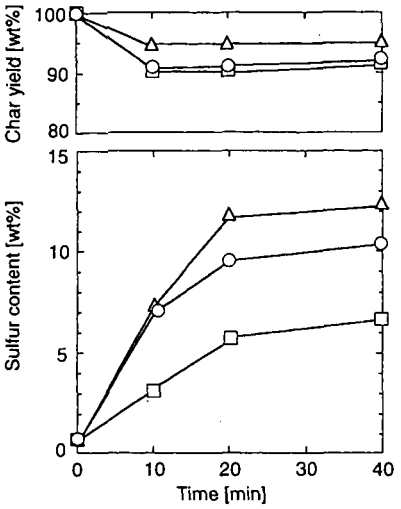

Fig. 4 Sulfur capture by Rosebud char in H_2S/N_2 stream at 1073 K. (Hydrogen sulfide conc.: □ ,0.29%; ○,1.01%; △, 2.91%)

ACKNOWLEDGMENT

The authors are grateful to Mr. Hiroaki Inoue for his assistance. This work was supported in a part by Basic Research Associate for Innovated Coal Utilization Program (NEDO).

REFERENCES

1) Kelemen, S. R..; George, G. N.; Gorbaty, M. L. *Fuel* **1990**, 69, 939-944

2) Kelemen, S. R.; Gorbaty, M. L.; George, G. N; Kwiatek, P. J.; Sansone, M. *Fuel* **1991**, 70, 369-402

3) Huffman, G. P..; Huggins, F. E.; Mitra, S.; Shah, N.; Pugmire, R. J.; Davis, B.; Lytle, F. W.; Greegon, R. B. *Energy Fuels* **1989**, 3, 200-205

4) Huffman, G. P.; Mitra, S.; Huggins, F. E.; Shah, N.; Vaidya, S.; Lu, F. *Energy Fuels* **1991**, 5, 574-581

5) Sugawara, K.; Tozuka, Y.; Sugawara, T.; Nishiyama, Y., *Fuel Process. Technol.* **1994**, 37, 73-85

6) Sugawara, T.; Sugawara, K., Nishiyama, Y.; Sholes, M. A. *Fuel* **1991**, 70, 1091-1097

7) Sugawara, K.; Gunji, T.; Sugawara, T.; Shirai, M.; Nishiyama, Y. *Energy Fuels*, **1997**, 11, 1272-1277

8) Sugawara, K.; Abe, K.; Sugawara, T.; Nishiyama, Y.; Sholes, M. A. *Fuel* **1995**, 74, 1823-1829

9) Sugawara, K.; Tozuka, Y.; Kamoshita, T.; Sugawara, T.; Sholes, M. A. *Fuel* **1994**, 73, 1224-1228

10) Sugawara, T., Sugawara, K.; Ohashi, H. *Fuel* **1989**, 68, 1005-1011

11) Sugawara, K.; Sugawara, T.; Shirai, M. *Jpn. J. Appl. Phys.* **1999**, 38, 608-611

XAFS STUDY OF SULFUR FORMS IN COALS DURING RAPID PYROLYSIS

Masayuki Shirai[1], Masahiko Arai[1], and Katsuyasu Sugawara[2]

[1] Institute for Chemical Reaction Science, Tohoku University,
Katahira, Aoba, Sendai, 980-8577, JAPAN
[2] Faculty of Engineering and Resource Science, Akita University,
1-1 Tegata Gakuen-cho, Akita City, Akita 010-8502, JAPAN

Keywords: Coal, Desulfurization, XAFS

ABSTRACT

Various kinds of coal, having the same average diameter and 89% C daf, were pyrolyzed rapidly in a free-fall reactor at atmospheric pressure under a nitrogen stream at a terminal temperature of 1253 K. The extent of organic sulfur removal in the rapid pyrolysis were different. Sulfur K-edge X-ray absorption near edge structure indicated that the organic sulfur species removed from coals were elemental, disulfide, sulfide and sulfoxide sulfur. The extent of organic sulfur removal in the rapid pyrolysis depended on the coals, because the amount and fraction of the volatile organic sulfur species were different even when the coals have the same carbon content.

1. INTRODUCTION

Sulfur is one of the most troublesome contaminants in coal. Although, present only in low concentrations, sulfur causes problems in every process that uses coal. When released into the atmosphere as SO_2 through combustion, it produces so-called acid rain. Certainly, a better understanding of the nature and distribution of sulfur-bearing minerals, organic sulfur-containing functional groups and their concomitant chemistry is necessary for improving advanced coal preparation processes and the environmental acceptability of coal-derived energy. Sulfur takes on several forms in coal including elemental, mineral and organic. Conventional coal cleaning technologies are grouped into physical and chemical methods. Because physical processes are limited to removal of inorganic constituents, development of an efficient process of organic sulfur removal is an urgent issue for sustainable resource development and environmental conservation. Development of a chemical desulfurization process requires a detailed understanding of organic sulfur forms in coal.[1] X-ray absorption near edge structure (XANES) spectroscopy has been shown to be a powerful method for the direct, nondestructive, and quantitative determination of organic sulfur-containing functional groups forms in coal.[2-4]

In the present study, dynamic behaviors of sulfur forms for several coals were followed in rapid pyrolysis. These coals were first served as a lumped sample which had the same average particle diameter without density separation. Then, the same samples were separated into three groups by a sink-float method to investigate effects of particle-density distribution on sulfur forms and their desulfurization behavior in rapid pyrolysis. Organic sulfur forms were determined by using XANES for the density-separated coals before and after pyrolysis.

2. EXPERIMENTAL

The coal samples were used in the experiment as soon as received. Average particle size of the sample was 0.35 mm. The samples were separated into three density groups by a sink-float method in zinc chloride aqueous solution. The absence of zinc chloride in the density-separated sample was confirmed by extraction with 5 M HCl for 2 h.

Rapid pyrolysis experiment was conducted by using a free-fall pyrolyzer. This apparatus enables coal particles to be heated in a nitrogen stream at rates from 10^3 to 10^4 K/s depending on particle density and diameter. Particle residence time is varied by changing the length of the heating section. The temperature was 1253 K at the isothermal section of the reactor.

Sulfur K-edge X-ray absorption near edge structure spectroscopy was applied to specifying the forms of organic sulfur in raw and char. XANES measurements were carried out at beam line 2A of Photon Factory in the National Laboratory for High Energy Physics. Si(111) monochromator was used to vary the incident X-ray energy. The beam irradiated the samples fixed on a nickel plate under 10^{-3} Pa in a vacuum chamber. Data were recorded in the fluorescence and electron yield modes in the region of the S K-edge at room temperature. The absolute photon energy was calibrated with the

assumption that the giant resonance of K_2SO_4 (S 1s $\rightarrow$ t2) appears at 2481.7 eV. The third derivatives of XANES spectra from model compounds were used as fingerprints for interpreting sulfur forms in the sample. Ferrous sulfide, pyrite, crystalline sulfur, DL-cystine, thioxane-9-one, S-methyl-L-cysteine, DL-methionine sulfoxide, and potassium sulfate were selected as the model compounds.

3. RESULTS AND DISCUSSION

Table 1 shows proximate, ultimate, and sulfur-form analyses for the sample coals. Figure 1 shows a correlation between extent of organic sulfur removal and carbon content for Nantong, Yanzhou, and Furong coals being studied in the present work, and for other 13 coals, carbon content ranging from 65 to 90% daf. The extent of organic sulfur removal is defined by

{1-(organic sulfur in char)/ (organic sulfur in raw coal)} $\times$ 100 (%)

where ultimate content of organic sulfur in the rapid pyrolyzed char based on coal basis was used as organic sulfur in char in this equation. By considering the thermal stability of thiophenic, and sulfide sulfur, it is plausible that the extent of organic sulfur removal decreases linearly with the increase of carbon content due to the increase of thiophenic sulfur content.

Table 1. Analyses of Sample Coals

	ultimate (wt %, daf)					proximate (wt%, db)		sulfur form (wt % of total sulfur)		
sample	C	H	N	S	diff	VM	ash	pyritic	sulfate	organic
Nantong	88.9	4.9	0.6	5.0	0.6	17.0	17.3	34	1	65
Yanzhou	89.1	5.5	1.1	3.2	1.1	43.2	9.1	38	1	61
Furong	88.9	3.1	0.9	6.6	0.5	10.5	21.6	77	0	23

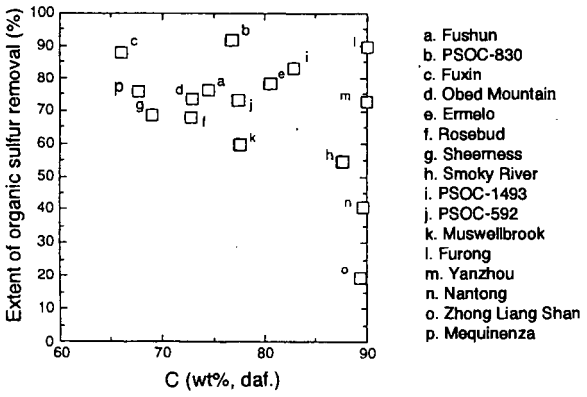

Figure 1. Change in extent of organic sulfur removal from solid phase with carbon content.

An apparent linear correlation, however, cannot be obtained between the extent of organic sulfur removal in rapid pyrolysis and carbon content of raw coals as demonstrated in Figure 1. The large difference from 19% to 89% of the extent of organic sulfur removal was noted for five kinds of high-rank coals containing more than 87% carbon. High-rank Furong coal was desulfurized to 89%, the second highest extent of desulfurization in 16 coals.

Figure 2 shows a relation between yield and density obtained by the sink-float method in zinc chloride aqueous solution. The density distribution differs from coal to coal even through carbon content is the same. The samples were separated into three groups with expected differential concentration of macerals.[5] The range of each group was altered in three kinds of coal to obtain enough amount of fractionated samples to be supplied for rapid pyrolysis experiments.

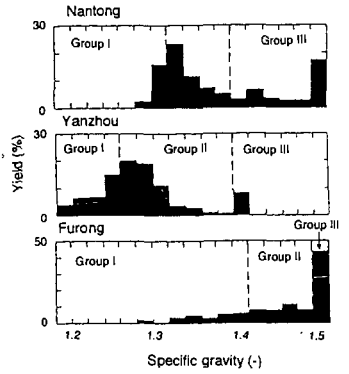

Figure 2. Yield distribution in density separation.

The raw and separated samples, group I, II, and III, were rapid pyrolyzed in a nitrogen stream with the free-fall reactor. Figure 3 represents a relation between the extent of organic sulfur removal and average density. Nantong and Yanzhou coals show linear relationship between the extent of organic sulfur removal and average density of the groups in each coal. This result implies that thermally stable organic sulfur increases with the increase on density. The existence of thermally stable organic sulfur is expected in the group III of Nantong and group II of Furong coals because of smaller extent of organic sulfur removal than volatile yield. Group I of Furong coal showed larger extent of organic sulfur removal than group II as the same tendency as the other coals though volatile yield was independent of average density. Exceptionally, more than 90% of the extent of organic sulfur removal was observed for group III of Furong coal, although the low extent of organic sulfur removal was expected because of high rank coal.

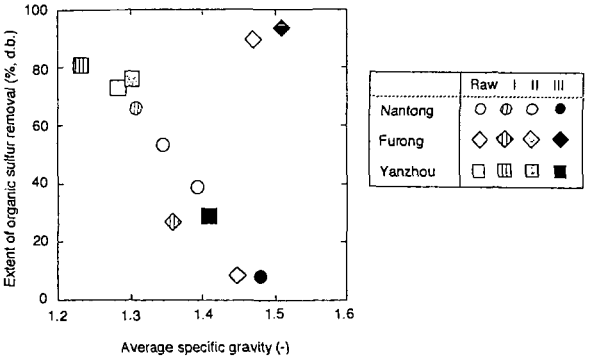

Figure 3. Change in organic sulfur removal with average density.

Figure 4 shows third differential curves of XANES spectra for groups I and III of Nantong coal. Strong peak is observed around 2472 eV for group I, which are attributable to thiophene and sulfide. A strong peak at 2474.5 eV results from sulfoxide. Through group III shows the similar distinct peaks of thiophene and sulfoxide to group I, the sulfide peak dose not appear for group III. It could be estimated that efficient desulfurization in a smaller density group such as group I is related to the presence of sulfide though the absolute amount of each sulfur form should be determined.

Third differential curves of XANES spectra for groups I and III of Furong coal are shown in Figure 5. Thiophene, sulfoxide, and pyritic sulfur are observed for group I as the same as the curves of Nantong, group I. On the other hand, the curves for group III of Furong are very different from that of group I. In addition to the peaks resulting from thiophene, sulfoxide, and sulfate, intensive peaks are observed at 2470.4-2470.8 eV, which are combined peaks attributable to pyritic sulfur and elemental sulfur. Figure 6 represents third differential curves of XANES spectra of rapid pyrolysis chars for group I and III of Furong coal. The curve of char for group I indicates that the sulfoxide peak becomes

smaller after pyrolysis while the peak of thiophenic sulfur remained. A peak at 2468.7 eV resulted from ferrous sulfide produced by reduction of pyrite. The peaks of pyritic sulfur and elemental sulfur disappeared and a large peak of ferrous sulfide at 2468.7 eV newly appeared after pyrolysis for group III. Furong coal has distinguishing characteristics as high organic sulfur content and removal extent of organic sulfur in larger density group III. XANES analysis, however, indicated that efficient extent of organic sulfur removal might be caused by releasing of elemental sulfur rather than organic sulfur.

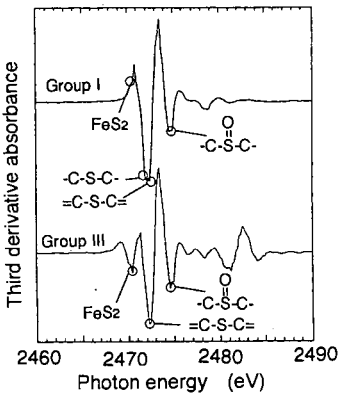

Figure 4. Sulfur K-edge XANES spectra of group I and III for Nantong coal.

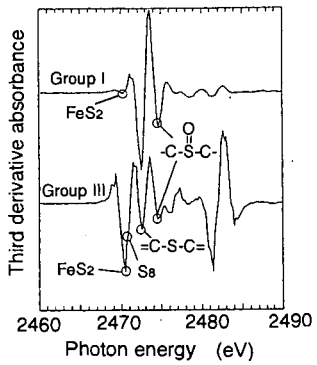

Figure 5. Sulfur K-edge XANES spectra of group I and III for Furong coal.

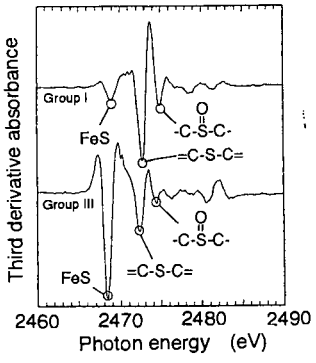

Figure 6. Sulfur K-edge XANES spectra of char for Furong coal.

4. Conclusion

In a serious on chemical coal cleaning, the desulfurization behavior in rapid pyrolysis was investigated for raw coals and their density-separated samples. The extent of organic sulfur removal shows linear decreasing tendency with the increase of density for each sample coal though the extent of organic sulfur removal was different from coal to coal even with the same carbon content. The high extent of desulfurization was estimated to be caused by elemental sulfur in the large density group of high-rank Furong coal.

References

(1) Davidson, R.M. *Fuel* **1994**, *73*, 988-1005.
(2) George, G. N.; Gorbaty, M. L. *J. Am. Chem. Soc.* **1989**, *111*, 3182-3186.
(3) Huffman, G. P.; Huggins, F. E.; Mitra, S.; Shah, N.; Pugmire, R. J.; Davis, B.; Lytle, F. W.; Greegor, R. B. *Energy Fuels* **1989**, *3*, 200-205.
(4) Shirai, M; Sugawara, K. *Inter. J. Mater. Eng. for Resources.* **1999**, *7*, 320-338.
(5) Sugawara, K.; Tozuka, Y.; Kamoshita, T,; Sugawara, T.; Sholes, M. A. *Fuel* **1994**, *73*, 1224-1228.

CHARACTERIZATION OF MICRO-DOMAIN STRUCTURE OF SOLVENT-SWOLLEN COAL BY SMALL ANGLE NEUTRON SCATTERING AND PROTON SPIN DIFFUSION

Koyo NORINAGA*, Masashi IINO, and George D. CODY†
Institute for Chemical Reaction Science, Tohoku University
Katahira, Aoba-ku, Sendai, 980-8577, Japan
†*Geophysical Laboratory, Carnegie Institution of Washington*
5251 Broad Branch Road, Washington, D. C. 20015

KEYWORDS: Coal, Swelling, Microphase separation

ABSTRACT

Blind Canyon coal was swollen by deuterated pyridine and was subjected to small angle neutron scattering (SANS) and ^{1}H NMR relaxation measurements. Based on the transverse relaxation characteristics, it was found that there exist at least two distinct structural regions in the swollen coals. However the measured longitudinal relaxation was best characterized by a single component as spin diffusion is rapid in the swollen coals. The dynamics of spin diffusion were revealed using a partially modified Goldman-Shen pulse sequence and analyzed by a simple mathematical model of a two phase system. The *interdomain spacing*, d_i, was estimated based on the diffusive path length for each spatial dimension. The d_i value evaluated under one-dimension was 15 nm and agreed with d_i determined by SANS, suggesting that the domain shape is sheet.

INTRODUCTION

The most convincing model of coal structure is that of a cross-linked macromolecular network. [1-5] The swelling of coal in various solvents has been studied to evaluate the molecular weight between cross-link points. [2, 4-8] The *Flory-Rehner theory* [9] has been frequently employed to relate the macromolecular network parameters to the degree of swelling in a good solvent. The theory assumes that the deformation is affine, i.e., the primitive chain is deformed in the same way as the macroscopic deformation (swelling) of the sample. Accordingly, the coal must swell uniformly in the segmental scale when we relate the macroscopic swelling to molecular characteristics such as the cross-link density. Based on the ^{1}H NMR transverse relaxation characteristics, however, it was found that the coal hydrogen in the pyridine-swollen state could be divided into two groups: those with relaxation characteristic of solids and those with relaxation characteristic of liquids. [10-17] Barton et al. [12] reported that up to 60 % of coal's macromolecular structure becomes mobile when immersed in deuteropyridine, while the remaining 40 % remains rigid as detected through ^{1}H NMR transverse relaxation measurements. Base on this finding, they first established that the swollen coal has a phase separated structure involving a solvent rich phase and an apparently solvent impervious phase.

Recently, Norinaga et al. [18] reported that the scale of the heterogeneity in the swollen coals. They characterized the phase separated structure of solvent swollen coal using its proton spin diffusion property. Five coals of different ranks were swollen by saturation with deuterate pyridine and were subjected to ^{1}H NMR relaxation measurements. The dynamics of spin diffusion were revealed using a partially modified Goldman-Shen pulse sequence and analyzed by a simple mathematical model of a two phase system. These calculations indicated that the solvent rich phase domains in the swollen coals range in size from several up to 20 nm. These results highlight the current limits in our understanding of the macromolecular structure of coals and place into question the use of affine models of strain for the interpretation of macroscopic swelling measurements. However the results depend on the spatial dimension of domains, i.e., the degree of freedom of the spin diffusion. Hence the information regarding the morphology of the domains is required to evaluate the domain size more precisely.

In the present study, the phase structure of a bituminous coal swollen by deuterate pyridine was characterized. In order to evaluate the morphology of the domains, we employ two different techniques. One is proton spin diffusion and the other is small angle neutron scattering(SANS). SANS gives an information on the average periodicity of the microphase structure, that is, the average distance between the centers of adjacent solvent-impervious-domains. It is possible to convert the size of the solvent rich phase into an interdomain spacing using an appropriate domain model. Thus the morphology of the domains can be evaluated by comparing the results of the spin diffusion with those of SANS.

EXPERIMENTAL

Samples. Blind Canyon coal supplied from Argonne Premium Coal Sample suite was used. The elemental composition of the dried Blind Canyon coal (hereafter referred to as BL) was C=80.7 wt %, H=5.8 wt %, N=1.6 wt %, S=0.4 wt %, and O=11.6 wt % on a dry-ash-free basis. [19] Their particle sizes were finer than 150 μm. 0.3 g of BL was weighed and transferred to an NMR tube with a 10 mm o.d. This tube was charged with per-deutero pyridine (Aldrich, 99.99% atom D), py-d_5, and sealed under a pressure of less than 2 Pa while frozen in liquid nitrogen. Solvent to coal mass ratio (S/C) ranged from 0.36 to 4.12. BL was exhaustively extracted in pyridine prior to SANS experiments. 0.15 g of sample

was loaded into a suprasil cyrindrical cell with 2 mm path length (vol = 0.7 mL). 0.6 mL of deuterated solvent (benzene / pyridine mixed solvent) was introduced to the cell.

SANS. SANS data were measured at the Intense Pulsed Neutron Source of Argonne National Laboratory, using the Small Angle Diffractometer (SAD). This instrument uses pulsed neutrons derived from spallation with wavelengths in the range of 0.1 - 1.4 nm and a fixed sample-to-detector distance of 1.54 m. The scattered neutrons are measured using a 64 x 64 array of position sensitive, gas filled, 20 x 20 cm^2, proportional counters with the wavelengths measured by time of flight by binning the pulse to 67 constant $\Delta t/t = 0.05$ time channels. The size range in a SANS experiment is constrained by both the geometry of the instrument and the wavelength of the neutrons which determine the working range of momentum transfer Q.

$$Q=4\pi\lambda^{-1}\sin\theta \qquad (1)$$

where θ is half the Bragg scattering angle and λ is the wavelength of the neutrons. Given the characteristics of the SAD at the Intense Pulsed Neutron Source (IPNS), useful SANS data in the Q range of 0.0006-0.025 nm^{-1} can be obtained in a single measurement. The reduced data for each sample is corrected for the backgrounds from the instrument, the suprasil cell, and the solvent as well as for detector nonlinearity. Data are presented on an absolute scale by using the known scattering cross-section of a silica gel sample.

^{1}H NMR. NMR measurements were carried out at 303 K using a JEOL Mu-25 NMR spectrometer equipped with a spin locking unit operating at a proton resonance frequency of 25 MHz. The solid-echo pulse sequence, [20] $90°_x$-τ-$90°_y$ (90° phase shift) provided an approximation to the complete free induction decay (FID). Typical values for the pulse width, pulse spacing, repetition time and number of scans were 2.0 μs, 8.0 μs, 6 s, and 32, respectively. The saturation recovery pulse sequence, $90°_x$-τ-$90°_x$, was used to monitor the recovery of the magnetization with the pulse separation time, τ and provided T_1. $T_{1\rho}$ was measured using a spin-locking pulse sequence, [21] that includes a $90°_x$ pulse followed by a reduced amplitude pulse, phase shifted 90°, and sustained for a variable time, t. The magnetization remaining at time t is monitored by observation of the free induction decay signal. The rotating frame measurements were made in a 6 G radiofrequency field. The spin diffusion was monitored with the Goldman-Shen pulse sequence. [22] In order to avoid the dead-time effect after the pulse, the original pulse sequence was modified as $90°_x$-τ_0-$90°_x$-t-$90°_x$-τ_1-$90°_y$, according to Tanaka and Nishi. [23]

RESULTS AND DISCUSSION

SANS results. The SANS data for a number of solutions of varying benzene to pyridine are presented in Figure 1. These data are presented as the log of the coherent scattering intensity, $I(Q)$, against the log of the momentum vector, Q. It is clear that there are significant changes in coherent scattering with increasing swelling ratio. These changes are relatively large scale. For example in the intermediate Q range around 0.02, $I(Q)$ increases by a factor of five with increased swelling (pyridine concentration in solution). It should be noted that Q~0.02 corresponds to a real space length of ~16 nm. It is noteworthy that at low Q, the effects of swelling are considerably less, thus the changes in coherent scattering "peak" in the intermediate Q range. Cody et al. [24] observed that similar creation of scattering intensity in the intermediate Q range with swelling of the Upper Freeport coal. In that work, they argued that the scattering at low Q was independent of scattering at intermediate Q. Thus, we concluded that the intermediate scattering was the results of an interparticle scattering phenomena as opposed to primary scattering of individual particles. The same interpretation can be applied here since the swelling of this coal is inhomogeneous, i.e., there exist solvent rich and solvent impervious domains as will be demonstrated by the ^{1}H NMR relaxation characteristics.

^{1}H NMR results. The FID curves for the swollen BL coal are drawn as a function of decay time in Figure 2. Although the solvent swelling enhances the fraction of slowly decaying components, a portion of the coal hydrogen remains rigid. For a dipole coupled rigid systems such as dry coal, the time decay of the nuclear magnetization can be characterized by a Gaussian function. On the other hand, in a liquid or a liquid-like environment, the magnetization decay is approximately an exponential function. Therefore the observed FID was assumed to be expressed by the following equation and was analyzed numerically by the nonlinear least squares method.

$$I(t) = I_G(0)\exp[-t^2/2T_{2G}^2] + I_{L1}(0)\exp[-t/T_{2L1}] + I_{L2}(0)\exp[-t/T_{2L2}] \qquad (2)$$

where $I(t)$ and $I_i(t)$ are the observed intensity at time t, and that attributed to component i, respectively, and T_{2i} is the transverse relaxation time of the i th component. The fractions of hydrogen producing exponential decays, f_{MH}, are plotted against S/C in Figure 3. f_{MH} was increased up to 0.5 with increase in S/C. However, f_{MH} kept almost constant value above S/C≈2.24, indicating that there exist the solvent impenetrable regions in the swollen coal even at S/C=4.72. For the swollen coal samples, it is clear that there are domains which do not swell and are not penetrated by solvent as shown schematically in Figure 4. The phase structures of the swollen coal are separated into at least two phase, i.e., solvent rich (SR)

and solvent impervious phase (SI).

To examine whether the spin diffusion process is active or not in the swollen coal samples, proton longitudinal relaxation was measured both in the laboratory and rotating frame. Table 1 lists the result of T_1 and $T_{1\rho}$ measurement for the swollen UF coal. T_1 is composed of one component while $T_{1\rho}$ can be analyzed by the sum of two exponential functions. From these results, one can clearly understand the effect of spin diffusion. T_2 signals are composed of three components without the effect of spin diffusion while $T_{1\rho}$ and T_1 measurements are affected strongly by spin diffusion and the number of the components decreases from $T_{1\rho}$ to T_1. The existence of at least two time constants for a rotating frame longitudinal relaxation process i.e., $T_{1\rho}$, in a system means that spin-diffusion processes cannot effectively average the different dynamical properties of protons in different spatial domains on the relevant time scale of the specific relaxation process. On the other hand, in the time scale of T_1 measurements, the distinctly separated spin systems were sufficiently averaged by the spin diffusion. The scale of spatial heterogeneities of the swollen coals can be estimated by evaluating the diffusive path length, i.e., the maximum linear scale over which diffusion is effective. The Goldman-Shen pulse sequence was thus employed to monitor the spin diffusion process. The advantage of the Goldman-Shen experiment is that the time for spin diffusion can be arbitrarily varied, and if this time is much less than T_1, the analysis is straightforward. The Goldman-Shen experiment is a technique to put the separate spin systems at different spin temperatures and then sample them as a function of time so that their approach to equilibrium can be followed. In Figure 5, the recovery factor of the magnetization of SI phase, $R(t)$, is plotted versus square root of time, $\tau^{1/2}$ for the solvent-swollen BL coals. S/C has almost no effects on the observed $R(t)$. The time evolution of $R(t)$ is analyzed by the diffusion equation solved by Cheung and Gerstein [25] to get information on the diffusive path length, l. The solid curves in Figure 5 represent the nonlinear least squares fits to the data by using the diffusion equation. The analytical fits give l to be 7, 16, and 25 nm for one, two, and three dimensions, respectively.

Comparison of SANS and ^{1}H NMR results. To compare the NMR results with SANS, we must convert the spin diffusion path length into an interdomain spacing. The spheres of SI phase are assumed to be covered with a uniform layer of SR phase of thickness l as shown in Figure 6. This model allowed to produce the following two equations,

$$l = r_C - r_{SI} \tag{3}$$

$$\phi_{SI} = \phi_C(1 - f_{MH}) = \left(\frac{r_{SI}}{r_C}\right)^d \tag{4}$$

where ϕ_{SI}, ϕ_C, and d are volume fractions of SI domains, volume fraction of coal in the swollen coal gel, and spatial dimension of the domain, respectively. In eq 4, we assumed that the hydrogen ratio is identical to the volume ratio. Twice r_c is taken to be equal to the interdomain spacing, d_i. d_i was estimated for each spatial dimension. The d_i evaluated under one-dimension at S/C=4 was approximately 15 nm and agreed with d_i determined by SANS, suggesting that the domain shape is sheet.

ACKNOWLEDGMENT. The authors are grateful to Drs. Tadashi Yoshida and Masahide Sasaki of the Hokkaido National Industrial Research Institute for their useful advice on the NMR measurements. This work was supported in part by a "Research for the Future Project" grant from the Japan Society for the Promotion of Science (JSPS), through the 148th Committee on Coal Utilization Technology.

REFERENCES

(1) van Krevelen, D. W. *Fuel* **1966**, *45*, 229.
(2) Green, T.; Kovac, J.; Brenner, D.; Larsen, J. W. In *Coal Structures*; Mayers,R. A., Ed.; Academic Press: New York, 1982.
(3) Brenner, D. *Fuel* **1985**, *64*, 167.
(4) Larsen, J. W.; Green, T. K.; Kovac, J. *J. Org. Chem.* **1985**, *50*, 4729.
(5) Lucht, L. M.; Peppas, N. A. *Fuel* **1987**, *66*, 803.
(6) Sanada, Y.; Honda, H. *Fuel* **1966**, *45*, 295.
(7) Kirov, N. Y.; O'Shea, J. M.; Sergeant, G. D. *Fuel* **1968**, *47*, 415.
(8) Nelson, J. R. *Fuel* **1983**, *62*, 112.
(9) Flory, P. J. *Principles of Polymer Chemistry*; Cornell University Press: Ithaca: NY 1953.
(10) Jurkiewicz, A.; Marzec, A.; Idziak, S. *Fuel* **1981**, *60*, 1167.
(11) Jurkiewicz, A.; Marzec, A.; Pislewski, N. *Fuel* **1982**, *61*, 647.
(12) Barton, W. A.; Lynch, L. J.; Webster, D. S. *Fuel* **1984**, *63*, 1262.
(13) Kamienski, B.; Pruski, M.; Gerstein, B. C.; Given, P. H. *Energy Fuels* **1987**, *1*, 45.
(14) Jurkiewicz, A.; Bronnimann, C. E.; Maciel, G. E. *Fuel* **1990**, *69*, 804.
(15) Jurkiewicz, A.; Bronnimann, C. E.; Maciel, G. E. High-Resolution ^{1}H NMR studies of Argonne premium coals. In *Magnetic Resonance in Carbonaceous Solids*; Botto, C. E., Sanada, Y., Eds.; Advances in Chemistry; American Chemical Society: Washington, DC, **1993**, *229*, 401.

(16) Yang, X.; Larsen, J. W.; Silbernagel, B. G. *Energy Fuels* **1993**, *7*, 439.
(17) Yang, X.; Silbernagel, B. G.; Larsen, J. W. *Energy Fuels* **1994**, *8*, 266.
(18) Norinaga, K.; Hayashi, J. i.; Chiba, T.; Cody, G. D. *Energy Fuels* **1999**, *in press.*
(19) Vorres, K. S. *User's Handbook for the Argonne Premium Coal Sample Program*; Argonne National Laboratory: Argonne: IL, 1993.
(20) Powles, J. G.; Mansfield, P. *Phys. Lett.* **1962**, *2*, 58.
(21) Hartmann, S. R.; Hahn, E. L. *Phys. Rev.* **1962**, *128*, 2042.
(22) Goldman, M.; Shen, L. *Phys. Rev.* **1966**, *144*, 321.
(23) Tanaka, H.; Nishi, T. *Phys. Rev. B* **1986**, *33*, 32.
(24) Cody, G. D.; Obeng, M.; Thiyagarajan, P. *Energy Fuels* **1997**, *11*, 495.
(25) Cheung, T. T. P.; Gerstain, B. C. *J. Appl. Phys.* **1981**, *52(9)*, 5517.

Table 1 Results of Proton Longitudinal Relaxation Measurements for Blind Canyon Coal Swollen in Deuterated Pyridine.

S/C [a]	$T_{1\rho}$[ms]		T_1[ms]
	$T_{1\rho}^{f}$ [b]	$T_{1\rho}^{s}$ [c]	
0	0.7(0.52)	4.8(0.48)	66(1.00)
0.36	-	-	65(1.00)
0.68	1.0(0.52)	5.7(0.48)	108(1.00)
1.03	1.3(0.59)	7.3(0.41)	104(1.00)
1.33	0.8(0.67)	5.3(0.33)	112(1.00)
1.67	1.7(0.62)	12.1(0.38)	128(1.00)
2.24	1.7(0.54)	12.9(0.46)	141(1.00)
2.57	1.8(0.55)	15.8(0.45)	145(1.00)
3.52	1.7(0.54)	16.1(0.46)	130(1.00)
4.72	1.8(0.52)	20.2(0.48)	144(1.00)

Values in parentheses; fraction of each component, [a] Mass ratio of solvent to coal [b] Fast. [c] Slow.

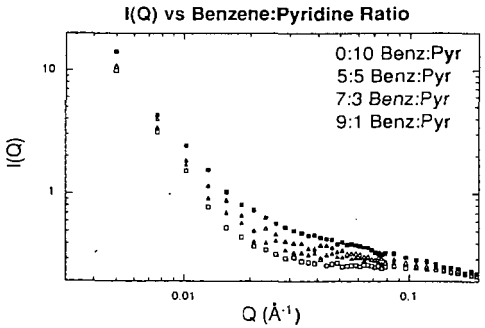

Figure 1 Coherent scattering intensity vs momentum vector for variably swollen BL residues in binary solvent of benzene-pyridine

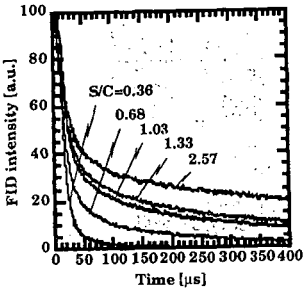

Fig.2 Transverse relaxation signals for pyridine swollen BL coal.

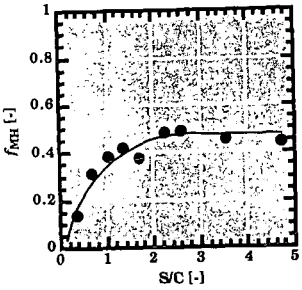

Fig.3 Change in f_{MH} with S/C.

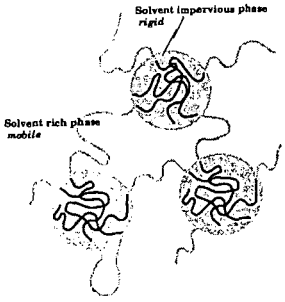

Fig. 4 Conceptual model for microdomain structure of solvent-swollen coal.

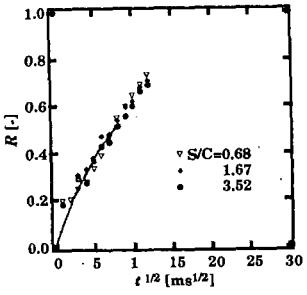

Fig.5 Recovery of proton magnetization in SI phase as a function of $t^{1/2}$ for the solvent-swollen BL coal. Solid lines represent the best fit to the data using a diffusion model.

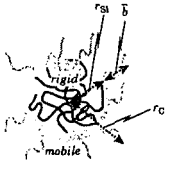

Fig.6 A 3-D domain model used to calculate the interdomain spacing from the spin diffusion distance.

SMALL ANGLE X-RAY SCATTERING STUDY OF COAL SOOT FORMATION

R. E. Winans, J. T. Parker†, S. Seifert, and T. H. Fletcher†

Chemistry Division, Argonne National Laboratory, Argonne, IL 60439
and †Chemical Engineering Department, Brigham Young University, Provo, UT 84602

Keywords: soot, SAXS, coal

ABSTRACT

The objective of this study is to examine, by small angle X-ray scattering (SAXS), the formation of soot from individual coal particle combustion in a methane flat flame burner. The SAXS instrument at the Basic Energy Sciences Synchrotron Radiation Center (BESSRC) at the Advanced Photon Source (APS) can be used to observe both the formation of spherules and clusters since it can access length scales of 6-6000 Å. The high X-ray flux enables rapid acquisition of scattering data of various regions of the flame. SAXS data reveal particle size, shape, surface areas, and surface roughness.

INTRODUCTION

Particulate formation in many types of combustion, such as in diesel engines and coal combustion, is a significant problem. For example, in coal combustion, soot formation control is important because of radiation heat transfer effects. The objective of this study is to observe in situ the formation of particles in flames using small angle X-ray scattering (SAXS). As a result of a DOE-BES Facilities Initiative (1), we have developed a high resolution SAXS instrument in the BESSRC-CAT at the Advanced Photon Source (APS). The SAXS facility offers new capabilities for measuring atomic order within disordered media, including combustion particulates, on a length scale of 6-6000 Å. A small research, flat flame burner has been constructed (2). The flux of photons from an undulator at the APS is needed to be able to observe the small number of soot particles in combustion of single coal particles.

We propose to look at the problem of particulate formation in coal combustion from the early growth stages to particulate agglomerate formation, all using SAXS. In an early in situ study (3) using SAXS to probe flames, the author noted that optical techniques had a lower limit of 600 Å while his instrument had an upper limit of 1000 Å. Typically, individual soot particles cluster to sizes starting at ~1000 Å. Optical methods can readily observe the clusters, but not the smaller spherules as they are formed. Our instrument can observe both the formation of spherules and clusters since it can access length scales of 6-6000 Å. SAXS data can reveal particle size, shape, surface areas, surface roughness and can provide information on the internal structure. This method provides complementary data to that obtained by optical methods.

Presently, a number of optical techniques are used to study soot in flames. Recently, Köylü (4) observed that there were large errors in determining soot particle size from light scattering. Also, the determination of properties were suspect due to uncertainties in soot refractive indices. However, thermophoretic sampling compiled with transmission electron spectroscopy (an ex situ method) has provided reliable size and shape information on the soot aggregates (4,5). These data can be used to help interpret the in situ SAXS results. Other optical techniques, such as laser induced fluorescence (6), have been used to analyze the pyrolysis process and especially to look at the polycyclic aromatic hydrocarbons, which are the probable precursors to soot.

A classic paper by Freltoft, Kjems, and Sinha (7) describes how power law correlations of small angle scattering can be used to describe clusters of small particles. A parameter called the fractal dimension (d_o) can be derived from this correlation. This value, d_o, relates how the mass of a cluster changes with a linear dimension. We have used this approach to examine coal derived molecules in pyridine with small angle neutron scattering data (8).

The experiments were conducted using a smaller version of a Hencken flat flame burner using a methane-air flame as the heat source. The coal particles are introduced individually through the center of the burner (5). It can be run fuel rich to observe pyrolysis or fuel lean to combust the coal particles. Other fuels, such as hydrocarbons, have been used with this burner. The burner is mounted on vertical and horizontal translation stages so that different parts of the flame can be probed.

EXPERIMENTAL

The SAXS instrument was constructed at ANL and used on the Basic Energy Sciences Synchrotron Radiation Center CAT undulator beamline ID-12 at the Advanced Photon Source (http://www.bessrc.aps.anl/). The SAXS instrument has been designed to minimize parasitic scattering which would interfere with scattering from dilute samples such as soots in flames. An important key to this feature of the instrument is that the beam is defined 20 m from the sample which reduces the problem of scattering from the defining slits. A schematic of the instrument is shown in Scheme 1.

Monochromatic X-rays (8.5 - 23.0 keV) are scattered off the sample and collected on a 9-element mosaic CCD detector (15 x 15 cm) with maximum of 3000 x 3000 pixel resolution with 10 sec exposure times (9). The scattered intensity has been corrected for absorption, the air scattering, and instrument background. The differential scattering cross section has been expressed as a function of the scattering vector Q, which is defined as $Q = (4\pi/\lambda) \sin \theta$, where λ is the wavelength of the X-rays and θ is the scattering half angle. The value of Q is proportional to the inverse of the length scale ($Å^{-1}$). The instrument was operated with two different sample-to-detector distances, 68.5 cm to obtain data at $0.04 < Q < 0.7$ $Å^{-1}$ and 3740 cm to measure at $0.006 < Q < 0.1$ $Å^{-1}$.

The Argonne Premium Coal Samples (10) used in this study were sized to the range of 45-75 μm. The burner used for these studies was a 1" x 1" axial symmetric flat flame burner produced by Research Technologies. The coal and liquids were fed through a tube centered in the burner and, a 0.25" nitrogen and helium co-flow around the perimeter was used to stabilize the methane/hydrogen flame. The individual coal particles were fed to the flame using a technique which that has previously been described (5). Liquid samples were introduced into the flame via a 0.25 μm fused silica tube which protruded 2 mm above the surface of the burner. Samples such as toluene and heptane were flowed into the flame at 0.1 ml using an automated syringe.

The burner was mounted on a x-y translational stage such that the flame could be moved through the X-ray beam both vertically and horizontally.

Small Angle X-ray Scattering

A typical plot of the scattering data for soot formation as a function of distance from the top of the burner of the Illinois No. 6 bituminous coal (APCS 3) is shown in Figure 1. These curves can be analyzed to determine size of features, topology, and changes in total scattering. Power law slope from the data, such as is shown in Figure 1, are used to describe the topology of the system. Finally, the invariant Q_0 is calculated and is proportional to the fluctuation of the electron density in the system. Changes in the invariant are useful in monitoring topological changes in the sample, $Q_0 = \int_0^\infty I(Q)\, Q^2\, dQ$. For example, the invariant goes to zero for a homogeneous system that does not have any concentration fluctuation.

RESULTS AND DISCUSSION

The scattering data were obtained as the burner was moved in 1 mm steps, such that the X-ray beam passed through the flame vertically from the bottom (0 mm) to 40 mm above the bottom. In addition, vertical sets of data were collected as the beam was positioned on center, where the coal particles emerged, and 1 ml increments from the center. The Illinois No. 6 (APCS 3) data from a vertical set at the center of the burner is shown in Figure 1. An initial Guinier analysis of this data suggests that the particle sizes are polydispersed over the section of the flame where soot is observed. Also, there are no systematic changes in the invariant. However, as can be seen in Figure 2, the power law slope is increasing. This suggests that there is a roughening in the soot particle surface. Note the large amount of scatter in the data. This may mean that a wide range of soot particles are observed, or else that there is merely a lot of scatter in the data. With combustion of the coal particles, the scattering decreased rapidly as the X-ray beam is moved away from the center (not shown) and becomes difficult to measure at 3 mm from the center.

Hydrocarbons, such as toluene, gave much better data in this system than coal particles. The flame conditions and the data acquisition parameters are the same in both cases, but apparently a much more stable soot cloud results from the direct infusion of the aromatic hydrocarbon. The power law slope data for the toluene ($Q = 0.016$ to 0.04) is shown in Figure 3. For the first 5-10 mm of the lower part of the flame, the value of $d_o = 2.0$, strongly suggests that larger polycyclic aromatic

expected, the scattering for the combustion of heptane (not shown) was much less than that for toluene.

CONCLUSIONS

Some of the initial results look promising, but we need a low flame temperature in order to observe the intermediate sized particles. This approach may reduce the polydispersity.

ACKNOWLEDGMENTS

This work was performed under the auspices of the Office of Basic Energy Sciences, Division of Chemical Sciences, U.S. Department of Energy, and use of the Advanced Photon Source was supported by BES-DOE, all under contract number W-31-109-ENG-38. The support of the BESSRC staff is appreciated, especially J. Linton, M. Beno, G. Jennings, and M. Engbretson.

REFERENCES

1. DOE-BES Facilities Initiative entitled "Development of a Facility at APS for Time-Resolved/Anomalous Small Angle X-ray Scattering: Applications in Condensed Matter Research," R. E. Winans, P. Thiyagarajan, R. K. Crawford, K. A. Carrado, and D. M. Tiede.
2. McLean, W. M.; Hardesty, D. R.; and Poll, J. H. Proc., 18th Symp. (Int'l.) Combust., 1213 (1980).
3. England, W. A. *Combust. Sci. and Tech.* **1986**, *46*, 83-93.
4. Köylü, Ü. Ö. *Combustion and Flame* **1996**, *109*, 488-500.
5. Ma, J.; Fletcher, T. H.; Webb, B. W. *Energy Fuels* **1995**, *9*, 802-808.
6. Ragucci, R.; De Joannon, M.; Cavaliere, A. Proc., 26th Symp. (Int'l.) Combust., Vol. 2, 2525-2531 (1996).
7. T. Freltoft, J. K. Kjems, S. K. Sinha, Phys. Rev. B. 33, 269-275 (1986).
8. Cody, G. D.; Thiyagarajan, P.; Botto, R. E.; Hunt, J. E.; Winans, R. E. *Energy Fuels* **1994**, *8*, 1370-1378 (1994).
9. Westbrook, E. M.; Naday, I. *Methods Enzymol.* **1997**, *276*, 244-268.
10. Vorres, K. S. *Energy Fuels* **1990**, *4*, 420-426.

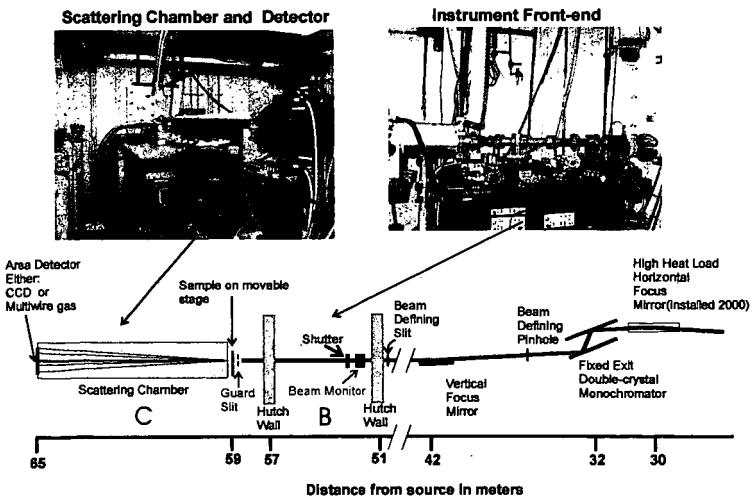

Scheme 1. TR/ASAXS Instrument on the APS BESSRC ID-12-B&C Undulator Beamline

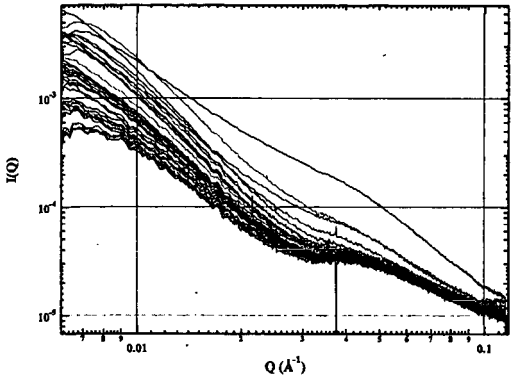

Figure 1. Scattering from Illinois coal (APCS 3) taken at 1 mm intervals from 0 to 40 mm above the top of the burner centered.

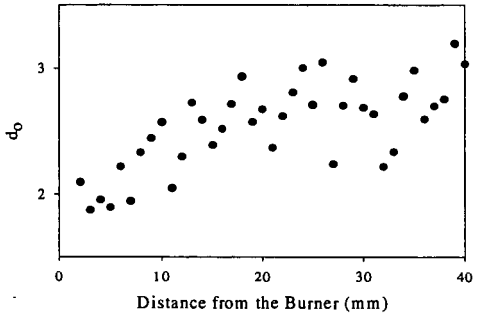

Figure 2. Power law slope from scattering of Illinois coal (APCS 3) soot taken along the centerline at 1 mm intervals from 0 to 40 mm above the top of the burner.

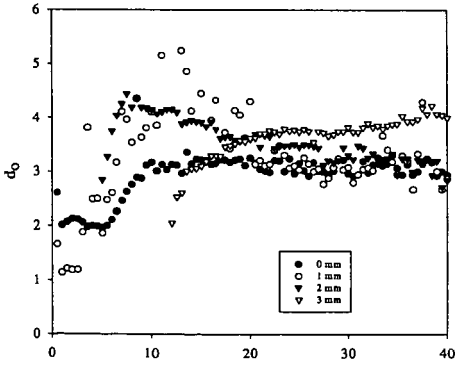

Figure 3. Power law slope from scattering of toluene soot taken at 1 mm intervals from 0 to 40 mm above the top of the burner at 1 mm intervals from the center.

For comparison, the nickel-impregnated coals were also prepared. About 1 g of raw coal was immersed in an aqueous solution containing about 6 or 12 wt % of nickel chloride and the water in this mixture was evaporated at 323 K under vacuum using rotary evaporator. The pH of the solution was controlled by using HCl or NH_3. The impregnated samples are identified using an additional code indicating impregnation (Im) and the pH at the time of impregnation, e.g., 10.51Ni (Im, pH3) for the specimen impregnated with 10.51 wt% nickel from solution of pH 3.

2.2 C1 Gas Analysis. The pyrolysis experiment was carried out in a fixed-bed-type pyrolyzer under helium flow at a heating rate of 5 K/min from 373 to 1173 K, and the evolved C1 gases were analyzed every 6 min by a gas chromatograph attached to the pyrolyzer.

2.3 Infrared Spectroscopy. Coal samples were diluted to 3 wt% by mixing of potassium bromide. Infrared spectra were obtained by diffuse reflectance method using a Perkin-Elmer 1600 Series FT-IR spectrometer.

2.4 XAFS. The details of procedure were described previously.[8-9] Briefly, data were collected at beam lines BL–7C, –10B, and –12C at the Photon Factory. Data were recorded in the transmission mode in the region of the Ni K edge (8331.7 eV) at room temperature. The transmission spectra were collected using ion chambers that were filled with nitrogen gas. EXAFS oscillation was extracted from the EXAFS raw data by using a cubic spline method and normalized with the edge height. The k^3-weighted EXAFS spectra were Fourier transformed to R space. The inversely Fourier filtering data were analyzed by a curve-fitting technique on the basis of the single-scattering plane-wave theory. Experimentally determined phase shifts and backscattering amplitudes for Ni-Ni and Ni-O were obtained from EXAFS data for Ni foil (Ni-Ni; coordination number (N) = 12, distance (R) =2.488 Å) and NiO (Ni-O; N = 6, R = 2.098 Å), respectively.

3. RESULTS AND DISCUSSION

3.1 C1 Gas Evolution. Typical C1 gas evolution profiles are given in Fig. 1. Obviously, the gas evolution was affected by the presence of nickel. The main features in the nickel-exchanged coals can be summarized as follows. The evolved CO gas shown in Figure 1(b) – (d) consisted of two peaks; one at 670 – 770 K and the other at around 920 K. When the nickel content was increased, the former peak shifted to lower temperature by 100 K but was almost the same in height. On the other hand, the latter peak height increased with the nickel contents, notably in the region below 3 wt%. For CO_2 evolution, it was seen that main peak shifted to lower temperature by 20 - 30 K compared to AW coal. The CO_2 evolution in the higher temperature region, above 800 K, was negligibly small for nickel content below 3 wt%, whereas the CO_2 in this region increased with the amount of nickel above 3 wt%. The CH_4 evolved profile had a small decrease in the middle temperature region between 720 and 870 K, possibly due to the nickel catalyzing secondary decomposition.

For nickel-impregnated coals, C1 gas evolution profiles are also shown in Figure 1. When the pH of the solution was low (Fig. 1(e)), C1 gas profile was similar to that of AW coal. On the contrary, C1 gas profile of sample prepared in the high pH of the solution (Fig. 1(f)) was similar to that prepared by ion exchange method.

The total gas evolution versus metal loading is presented in Fig. 2. The filled marks in this figure indicate the gas evolution from the impregnated coal. The effects of metal observed here consist of those metal-catalyzed decomposition of functional groups and the secondary conversion of oxygen containing volatiles into CO and CO_2 catalyzed by metal elements. From this figure, CO yields remarkably increased from 8% to 15% with increasing nickel loadings from 0 to about 3 %, whereas CO_2 yields were almost constant at about 7% in the same region of nickel contents. Above 3wt% of nickel loadings, CO and CO_2 yields gradually increased. It seems that the exchanged nickel below and above about 3 wt% differ somewhat in the way it affects the decomposition, whereas the impregnated nickel behaved quite differently and yielded less gases than the exchanged nickel.

These differences can be ascribed to a different state of nickel species. In the case of ion exchange, nickel ions are associated with carboxyl groups. On the other hand, most of nickel species loaded by impregnation method would form a cluster of the metal salt and, upon decomposition, distribute over the entire coal surface and not limited specifically to functional group sites. Therefore, it is likely that the exchanged nickel ions have a stronger influence than the impregnated species on the decomposition of functional groups in coal.

3.2 *States of nickel species after ion exchange.* For the nickel-exchanged coals, it is very interesting to change the pyrolysis behavior below and above 3 wt% of nickel loadings. In order to examine the chemical state of the exchanged nickel ions in brown coal, FT-IR measurement was carried out. Figure 3 shows the IR spectra of brown coals with various

exchanged nickel contents. The differences of IR spectra between AW and the nickel-exchanged coal are also shown in this figure. From this figure, it was found that the absorption band of carboxyl groups, which appeared at 1720 cm^{-1}, decreased with increasing nickel contents. On the contrary, the bands of OCO asymmetric stretching (ν_a) at 1550 cm^{-1} and OCO symmetric stretching (ν_s) at 1480 – 1410 cm^{-1} of carboxylate groups increased. It should be noted that the peak position of ν_s band depended on the amount of the exchanged nickel. The peak at 1480 cm^{-1} in low nickel loaded sample was dominant, but in high nickel loaded sample the peak at 1410 cm^{-1} was dominant. This suggests that the chemical state of nickel species differs by the nickel content. According to reference, it was found that this difference of peak position corresponded with the difference of the structure of carboxylate groups; the nickel ions in low loaded sample were associated with carboxyl groups in the form of bidentate-type, while those in high loaded sample were in the form of bridge-type.

3.3 EXAFS. To examine how such differences in the chemical form of nickel species influence on the behavior of nickel species during pyrolysis, EXAFS experiments was carried out. Figure 4 shows the Fourier transforms for EXAFS spectra of the 0.77Ni and 6.4Ni samples pyrolyzed from 373 to 853 K. From Fourier transformed EXAFS spectra of both nickel exchanged coals at 373 K, only Ni-O bond appeared between 1 and 2 Å was observed, indicating that the nickel species were highly dispersed on the brown coal surface independent of nickel loadings. The intensity of Ni-O bond decreased with increasing heat treatment temperature, while new peak around 2.5 Å, which was attributed to Ni-Ni bond, was appeared and its intensity increased. That is, the divalent nickel ions were reduced to the metallic state during pyrolysis. More interestingly, the transition temperature from divalent cations to metal particles depended on the nickel contents. Figure 5 shows the dependence of Ni-Ni coordination numbers on the pyrolysis temperatures. Nickel species in the low loaded sample aggregated to metal particles at 750 K. On the other hand, nickel species aggregated at 650 K in the high loaded sample. The transition temperature for the low loaded sample was 100 K higher than that of the high loaded sample. These transition temperatures corresponded with temperatures of the former CO peak described previously, which appeared at 770 K in the low loaded sample and at 670 K in the high loaded sample. The peak shift at about 100 K suggests that the states of nickel species in coal and their effects are different according to the nickel amounts. We suppose that the metallic nickel particle formation is related to the decomposition of carboxyl groups / CO evolution.

4. CONCLUSIONS

The following conclusions are obtained in this study.

(1) At the initial stage of pyrolysis, the exchanged nickel influenced on the decomposition of functional groups.

(2) The chemical structure of nickel carboxylate groups differs by the nickel content; the nickel ions in low loaded sample were associated with carboxyl groups in the form of bidentate-type, while those in high loaded sample were in the form of bridge-type.

(3) By using XAFS technique, the aggregation temperature of nickel species, which was 750 K at low loaded sample, was observed to have shifted to lower temperature by 100K at high loaded sample.

References

(1) Otake, Y., and Walker Jr., P. L., *Fuel*, **72** (1993) 139.
(2) Tyler, R. J., and Schafer, H. N. S., *Fuel*, **59** (1980) 487.
(3) Franklin, H. D., Peters, W. A., and Howard, J. B., *Fuel*, **61** (1982) 155.
(4) Schafer, H. N. S., *Fuel*, **58** (1979) 667.
(5) Schafer, H. N. S., *Fuel*, **58** (1979) 673.
(6) Murakami, K., Shirato, H., Ozaki, J., and Nishiyama, Y., *Fuel Process. Tech.*, **46** (1996) 183.
(7) Murakami, K., Ozaki, J., and Nishiyama, Y., *Fuel Process. Tech.*, **43**, (1995) 95.
(8) Shirai, M., Murakami, K., and Nishiyama, Y., *Energy Fuels*, **11** (1997) 1012.
(9) Shirai, M., Arai, M., and Murakami, K., *Energy Fuels*, **13** (1999), 465.

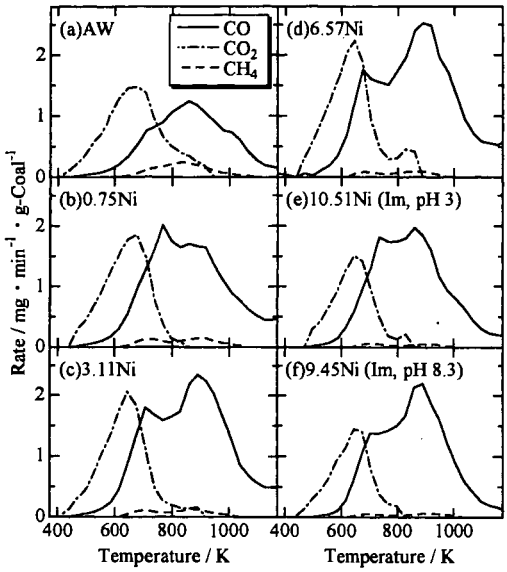

Figure 1. C1 gas evolution profiles of AW, nickel-exchanged coals, and nickel-impregnated coals.

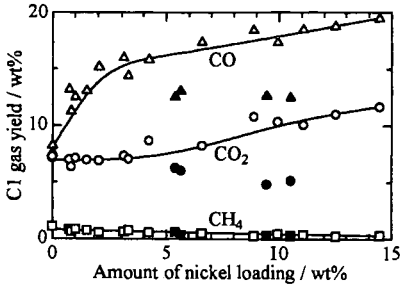

Figure 2. Change of C1 gas yields with the amount of nickel loading. Filled marks indicates impregnated samples.

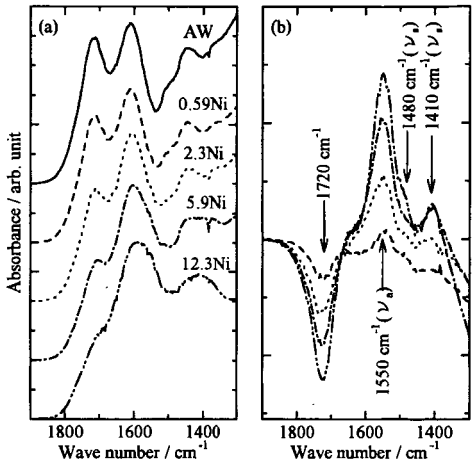

Figure 3. (a) IR spectra and (b) difference spectra of the nickel exchanged coals.

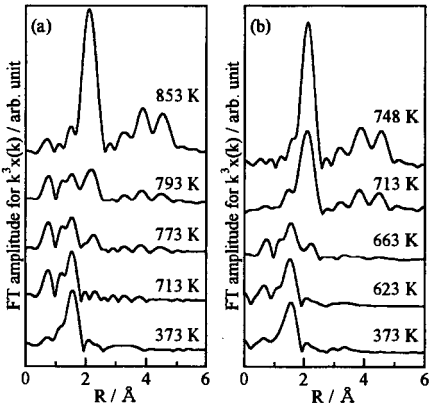

Figure 4. Fourier transforms for EXAFS oscillations of (a) 0.77Ni and (b) 6.4Ni nickel-loaded brown coals treated at several temperatures. These distributions were obtained by the Fourier transforms of the k^3-weighted EXAFS data.

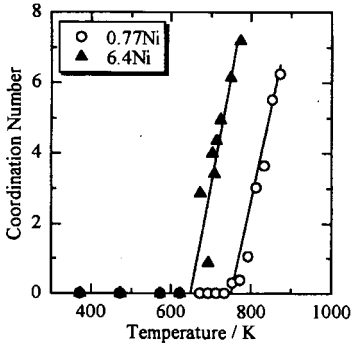

Figure 5. Coordination numbers of Ni-Ni bonds as a function of treatment temperature.

INFLUENCE OF ION-EXCHANGED NICKEL ON PYROLYSIS OF LOY YANG BROWN COAL

Kenji Murakami[1], Kiyoshi Fuda[1], Toshiaki Matsunaga[1], and Masayuki Shirai

[1] Department of Materials-process Engineering & Applied Chemistry for Environments, Faculty of Engineering and Resource Science, Akita University, Akita 010-8502, Japan
[2] Institute for Chemical Reaction Science, Tohoku University, Aoba-ku, Sendai 980-8577, Japan

Keywords: Pyrolysis, Ion-Exchanged Nickel, XAFS

ABSTRACT

Influence of ion-exchanged nickel on pyrolysis of Loy Yang brown coal was examined, partly using the X-ray absorption fine structure (XAFS) technique. Pyrolysis experiments were carried out up to 1173 K at 5 K/min in helium flow. CO yields remarkably increased from 8% to 15% with increasing nickel loadings from 0 to about 3 %, whereas CO_2 yields were almost constant at about 7% in the same region of nickel contents. Above 3wt% of nickel loadings, CO and CO_2 yields gradually increased. The peak of CO evolution in the acid-washed coal, without any nickel ions, was broad at 870K. On the contrary, the peak of CO was divided into two by the loading of nickel ions. First peak, which appeared at 670-770K, shifted to lower temperature with increasing ion-exchanged nickel, while second peak appeared at about 920K independent of the amount of nickel ions. Further, by using the XAFS technique; it was shown that the nickel species aggregated to metal particles at 750K in the case of low loaded sample and that the aggregation of nickel species shifted to lower temperature by 100K at high loaded sample.

1. INTRODUCTION

The pyrolysis behavior of brown coals and lignites on heat treatment has been studied extensively.[1-3] The initial stage of pyrolysis is thought to consist of decomposition of several functional groups. The thermal decomposition of functional groups affects significantly the initial stage of coal liquefaction, gasification, and pyrolysis, where several structural changes take place simultaneously. Particularly, it is very important to understand the effects of the ion-exchanged metal species, which are associated with mainly carboxyl groups, on the decomposition process, since these cations are well known to be good catalysts for coal conversion processes. Schafer investigated the relation between the decomposition of functional groups and the evolved gas during pyrolysis of acid-washed coal and alkali or alkaline earth metal exchanged coals.[4-5] He presented that CO and CO_2, which were evolved from the acid-washed coal during heat treatment, originated from phenolic hydroxyl groups and carboxyl groups, respectively. In the case of the cation-exchanged coals, other oxygen-containing groups associated with carboxyl groups yielded CO_2 before the carboxylate groups decomposed into CO_2, that is, the presence of metal cation stabilized carboxylate groups. However, the details of the decomposition process are still not understood.

We reported previously that the temperature of the C1 gas evolution as well as the C1 gas yields during the pyrolysis of the nickel-exchanged coal changed by their loadings.[6] This result suggests that the catalytic properties depend on the structure of active species during pyrolysis. The purpose of this study is to examine the influence of ion-exchanged nickel on pyrolysis of Loy Yang brown coal, partly using the X-ray absorption fine structure (XAFS) technique, which can provide information on local structure of highly dispersed catalytic species in coal.

2. EXPERIMENATAL

2.1 Sample Preparation. Loy Yang brown coal from Victoria, Australia, was used in this study. Raw coal was ground smaller than a 250 μm particle size, washed with deionized water, dried at 323 K under vacuum, and stored in a desiccator. The analyses for this coal are as follows: C: 67.6 % (daf), H: 5.2 % (daf), N: 0.8 % (daf), O: 26.4 % (diff), and ash: 0.2 % (dry). Acid-washed coal (AW) was prepared by stirring the raw coal in 0.5 mol/l of hydrochloric acid for 24 h. The concentration of carboxyl groups was 3.7 mmol/g.[7] About 10 g of the coal sample in 500 ml of an aqueous solution of nickel chloride at a concentration of 0.1 mol/l was stirred, and the pH of the solution was adjusted by adding ammonia or hydrochloric acid. After the pH remained unchanged for 5 h, the exchange reaction was judged to be equilibrium. The extent of exchanged nickel cation was determined by extracting the cation from the sample by hydrochloric acid. The nickel cation-exchanged samples are identified by the amount of loading (wt %), e.g., 0.75Ni for 0.75 wt% nickel-exchanged coal (daf).

WAVELENGTH DISPERSIVE X-RAY FLUORESCENCE SPECTROMETRY AS A TOOL TO STUDY THE EFFECTS OF PYRIDINE ON THE INORGANIC MOIETIES IN THE ARGONNE PREMIUM COALS.

David L. Wertz and Stephen S. DuBose
Department of Chemistry & Biochemistry
University of Southern Mississippi
Hattiesburg, MS 39406 USA
david.wertz@usm.edu

KEYWORDS. Gels, Pyridine, Inorganics

INTRODUCTION. Several manuscripts have appeared within the time frame of the Argonne Premium Coals Sample Program which have addressed the inorganic moieties contained in these coals. At the same time, numerous studies of the effects of liquids on the micro- and macro-level structuring in coals have been undertaken. This group, using x-ray diffraction, helped define the crystalline moieties in the APC's and, using x-ray scattering methods, has been studying the effect(s) of the additions of liquids on the average inter-layer distance for several of the coals. For many of these studies (including ours), pyridine has been of the liquids receiving primary focus - perhaps because of its polarity and its ability to form hydrogen-bonds. In addition, its aromaticity (and thus planarity) offers other possibilities for interactions with the organic moieties in coals. However, these same structural features cause pyridine to be an effective ligand towards metal ions – particularly the soft metal cations found in coals; and a extensive coordination chemistry exists using pyridine as either the solvent, and an inner-coordination sphere ligand, or both. In addition, pyridine has the capability to interact with both "inorganic" and "organic" sulfur. Consequently, the abundances of important inorganic species such as FeS_2 may be effected by the presence of excess pyridine. Presented below are the first results of a study of the gels produced by reacting pyridine with the APC's.

Experimental. 25 Mls of anhydrous pyridine (Aldrich) were added to a 5 grams (-100 mesh) sample of each of the Argonne Premium Coals. Each sample was allowed to equilibrate for 10-14 days. At the end of this period, the gels formed from the coal-pyridine interactions was separated from the remaining liquid by filtration. Each gel was air-dried and then mounted onto a sampleholder. A wavelength dispersive x-ray fluorescence (WDXRF) spectrum was obtained by irradiating each gel with rhodium Xrays (from an end-centered x-ray tube). The secondary Xrays emitted by each gel were focussed onto a graphite monochromator (d = 3.342 Å). The WDXRF spectrum was obtained by accumulating intensity data for 4 seconds at angular increments of $\Delta 2\theta$ = 0.05° over the angular range from 2θ = 8.00° to 140.00°. In terms of the wavelength and the energy of the secondary Xrays, this angular region corresponds to:

2θ	λ	ϵ
8.00°	0.47 Å	26.4 keV
140.00°	6.30 Å	1.97 keV

For comparison purposes the WDXRF spectrum of each of the APC's was also obtained.

RESULTS. Shown in Figure 1 are the superimposed WDXRF spectra of the eight Argonne Premium Coals. These spectra indicate the advantages of the wavelength dispersive method, good peak resolution and good signal/noise ratio. These spectra indicate that the eight APC's contain many of the same inorganic atoms, but in considerably different proportions. Principal among these are iron, calcium, and sulfur – which represent the major components. In addition, small peaks due to either titanium and/or potassium also appear in at least two of the spectra. These spectra verify the existence of the inorganic moieties previously reported.

The intensity of a specific peak in the WDXRF spectrum of a sample containing many components may be written as:

$$I_A(\lambda_A) = \eta_A \bullet M(\lambda_A) \bullet I^*_A(\lambda_A) \bullet \exp(-t_S \bullet \{\rho_S \bullet [\mu_S(\lambda_{Rh}) + \mu_A(\lambda_A)]\}). \quad (1)$$

In eq 1, $I_A(\lambda_A)$ is the intensity, typically in counts or counts per second, measured in the XRF spectrum and due to ana abundance of η_A of analyte A in the sample S. The efficiency of the spectrometer for detecting Xrays at wavelength λ_A is given by M. $I^*_A(\lambda_A)$ is the absorption and enhancement-corrected intensity due to 100% analyte A and may frequently be determined by iterative methods. The exponential includes several factors and is typically referred to as the matrix absorption effect(s). Among these factors are the mass absorption coefficients of the sample for the incident Rh Xrays and the mass absorption coefficient for the secondary Xrays

produced by analyte A, the density of the sample (ρ_S) and the thickness of the sample (t_S). Using mixtures of model compounds, the product of M•I* is being determined for a number of the important analytes in these coals. In addition, the sample thickness is controlled by the opening in the sampleholder. Consequently, for comparisons, several of the parameters noted in eq 1 may be eliminated from further considerations.

Shown below is the WDXRF spectrum of an Argonne Premium coal compared to the WDXRF spectrum of the gel formed when that coal has been treated with pyridine. A summary of the analysis of the intensity under the iron K_α peak, the calcium K_α peak, and the sulfur K_α peak is presented in Table I.

TABLE I. COMPARISON OF PEAK INTENSITIES.

COAL	PEAK INTENSITIES IN COUNTS PER SECOND					
	Fe PEAK @ 1.94 Å		Ca PEAK @ 3.36 Å		S PEAK @ 5.37 Å	
	Coal	Gel	Coal	Gel	Coal	Gel
APC 101	19,083	15,007	2,181	1,822	2,005	1,734
		-21%		-16%		-14%
APC 301	33,594	28,227	4,790	4,302	5,785	4,553
		-16%		-10%		-21%
APC 401	16,008	10,451	2,026	1,388	4,089	2,621
		-35%		-31%		-36%

Comparison show that the peaks intensities for these inorganics parallel their previously reported abundances, verifying the accuracies of the WDXRF method used in these experiments -- at least at a semi-quantitative level.

Peak intensity comparisons also show that in the transformation from the coal to the gel, the intensity of each peak is reduced -- by approximately the same amount. Each intensity reduction indicates that the abundance of each of these key inorganic moieties is also decreased. However, the cause(s) of the reductions in peak intensities has not been established unequivocally. This uncertainty in interpretation of the WDXRF spectra is because of the versatility of pyridine in its reaction(s) with coal. Specifically, it is known that pyridine causes coals to swell, which at the molecular level, is consistent with a change in the density of a powdered sample. The inclusion of pyridine into the organic matrix of the coal to form the gel causes a reduction in the abundances of the inorganic moieties in the coal. Both the change in abundances and the density change will affect the intensity of the analyte in an exponential manner. In addition, pyridine may complex with one (or more) of the inorganic analytes in the coal in such a manner as to be removed from the gel which is formed upon pyridine addition, thus causing a reduction in the abundance of that analyte.

Figure 1. WDXRF spectra of the Argonne Premium Coals.

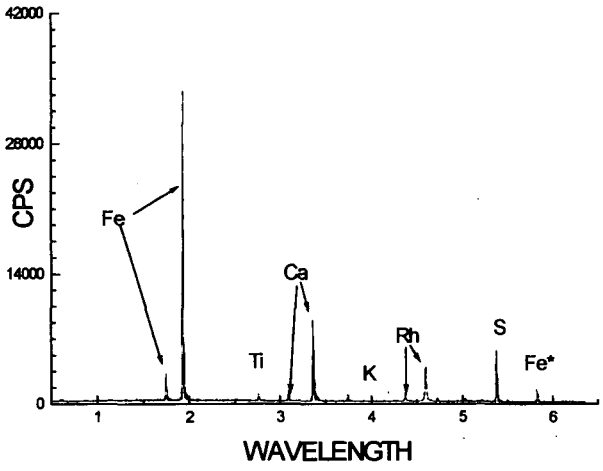

Figure 2. WDXRF spectra of APC 101 and its gel formed with pyridine.

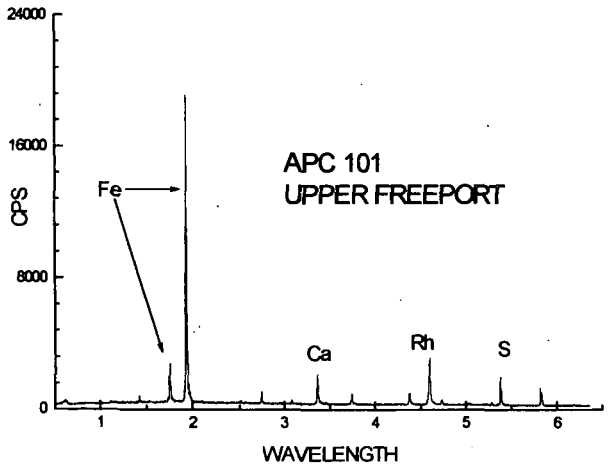

Figure 3. WDXRF spectra of APC 301 and its gel formed with pyridine.

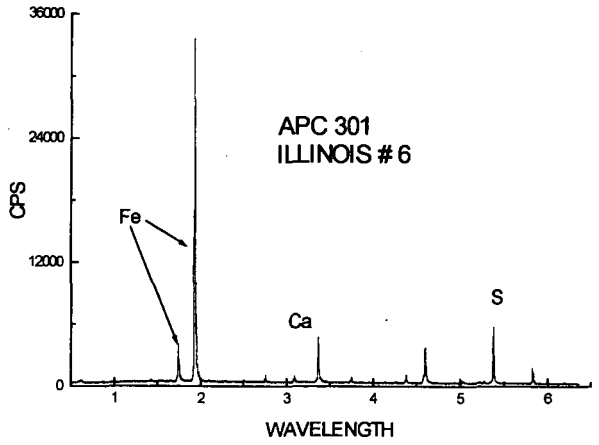

Figure 4. WDXRF spectra of APC 401 and its gel formed with pyridine.